

Elsevier Editorial System(tm) for Journal of Contaminant Hydrology  
Manuscript Draft

Manuscript Number: CONHYD2870R3

Title: Hydrogeophysical Imaging of Deposit Heterogeneity and Groundwater Chemistry Changes during DNAPL Source Zone Bioremediation

Article Type: Research Paper

Keywords: Bioremediation; DNAPL; Electrical resistivity tomography (ERT)

Corresponding Author: Dr Jonathan Edward Chambers, Ph.D, M.Sc, B.Sc.

Corresponding Author's Institution: British Geological Survey

First Author: Jonathan Edward Chambers, Ph.D, M.Sc, B.Sc.

Order of Authors: Jonathan Edward Chambers, Ph.D, M.Sc, B.Sc.; Paul B Wilkinson; Gary P Wealthall; Meng H Loke; Rachel Dearden; Ryan Wilson; Debbie Allen; Richard D Ogilvy

Abstract: Robust characterization and monitoring of dense nonaqueous phase liquid (DNAPL) source zones is essential for designing effective remediation strategies, and for assessing the efficacy of treatment. In this study high-resolution cross-hole electrical resistivity tomography (ERT) was evaluated as a means of monitoring a field-scale in-situ bioremediation experiment, in which emulsified vegetable-oil (EVO) electron donor was injected into a trichloroethene source zone. Baseline ERT scans delineated the geometry of the interface between the contaminated alluvial aquifer and the underlying mudstone bedrock, and also the extent of drilling-induced physical heterogeneity. Time-lapse ERT images revealed major preferential flow pathways in the source and plume zones, which were corroborated by multiple lines of evidence, including geochemical monitoring and hydraulic testing using high density multilevel sampler arrays within the geophysical imaging planes. These pathways were shown to control the spatial distribution of the injected EVO, and a bicarbonate buffer introduced into the cell for pH control. Resistivity signatures were observed within the preferential flow pathways that were consistent with elevated chloride levels, providing tentative evidence from ERT of the biodegradation of chlorinated solvents.

1           **Hydrogeophysical Imaging of Deposit Heterogeneity and Groundwater**

2           **Chemistry Changes during DNAPL Source Zone Bioremediation**

3                           Chambers, JE<sup>1</sup>, Wilkinson, PB<sup>1</sup>, Wealthall, GP<sup>1</sup>, Loke, MH<sup>2</sup>,

4                           Dearden, R<sup>1</sup>, Wilson, R<sup>3</sup>, Allen, D<sup>1</sup>, Ogilvy, RD<sup>1</sup>

5                           <sup>1</sup>British Geological Survey, Keyworth, Nottingham, UK, NG9 2ER

6                           <sup>2</sup>Geotomo Software Sdn. Bhd., 115, Cangkat Minden Jalan 5, Minden Heights, 11700 Gelugor, Penang, Malaysia

7                           <sup>3</sup>University of Sheffield, Department of Civil and Structural Engineering, Broad Lane, Sheffield, UK, S3 7HQ

8                           **ABSTRACT**

9           Robust characterization and monitoring of dense nonaqueous phase liquid (DNAPL) source  
10           zones is essential for designing effective remediation strategies, and for assessing the efficacy  
11           of treatment. In this study high-resolution cross-hole electrical resistivity tomography (ERT)  
12           was evaluated as a means of monitoring a field-scale in-situ bioremediation experiment, in  
13           which emulsified vegetable-oil (EVO) electron donor was injected into a trichloroethene  
14           source zone. Baseline ERT scans delineated the geometry of the interface between the  
15           contaminated alluvial aquifer and the underlying mudstone bedrock, and also the extent of  
16           drilling-induced physical heterogeneity. Time-lapse ERT images revealed major preferential  
17           flow pathways in the source and plume zones, which were corroborated by multiple lines of  
18           evidence, including geochemical monitoring and hydraulic testing using high density  
19           multilevel sampler arrays within the geophysical imaging planes. These pathways were  
20           shown to control the spatial distribution of the injected EVO, and a bicarbonate buffer  
21           introduced into the cell for pH control. Resistivity signatures were observed within the  
22           preferential flow pathways that were consistent with elevated chloride levels, providing  
23           tentative evidence from ERT of the biodegradation of chlorinated solvents.



---

1 2007). Where significant subsurface heterogeneity exists, conventional intrusive  
2 investigations and groundwater sampling can be insufficient, as the information they provide  
3 is restricted to vertical profiles at discrete locations, with no information between sample  
4 points. Therefore significant uncertainty can remain, in relation to the lithological variability,  
5 and in the distribution of DNAPL, electron donor or other amendment fluids. In order to  
6 mitigate this problem complementary geophysical ground investigation methods are now  
7 emerging (US EPA, 2004), as they have the advantage of producing spatial or volumetric  
8 information on subsurface variability, and can be sensitive to changes caused by the injection  
9 of amendment fluids (Lane et al., 2004; Hubard et al., 2008; Williams et al., 2009). Examples  
10 of field scale geophysical monitoring of DNAPL bioremediation experiments are, however,  
11 rare; previous studies are described by Daily and Ramirez (1995), who used cross-hole  
12 electrical resistivity tomography (ERT), with a spatial resolution of a few m<sup>2</sup>, to monitor  
13 methane electron donor injection at a TCE contaminated site, and Lane et al. (2006) who  
14 applied cross-hole radar methods for monitoring spatial and temporal distribution of EVO at  
15 a TCE and dichloroethene (DCE) contaminated site.

16 In this study cross-hole ERT was used as a means of imaging the subsurface during a  
17 pilot-scale experiment to monitor the bioremediation of a TCE source zone. The geophysical  
18 study formed a component of a wider experiment, which was designed to test the hypothesis  
19 that enhanced anaerobic bioremediation by reductive dechlorination can result in the effective  
20 treatment of chlorinated solvent DNAPL source areas (Zeeb et al., 2008). The specific  
21 objectives of the geophysical imaging described in this paper were to assess the efficacy of  
22 cross-hole ERT as a means of characterizing geological and hydrogeological heterogeneity,  
23 and monitoring changes in groundwater chemistry associated with the injection of EVO  
24 electron donor and bicarbonate buffer used for pH control, and chloride released through the  
25 biodegradation of chlorinated solvents. Here a novel experimental design was employed,

---

1 involving ERT arrays and multilevel groundwater sampling (MLS) arrays installed in closely  
2 spaced boreholes, which formed monitoring transects in both the source and plume zones.  
3 These arrays were designed to complement the detailed geochemical point sampling by  
4 providing geophysical imaging at a resolution (i.e.  $\text{dm}^2$ ) approaching that of the geological  
5 heterogeneity indicated during drilling.

## 6 **2. ELECTRICAL RESISTIVITY TOMOGRAPHY (ERT)**

7 ERT is a geophysical imaging technique that is used to generate 2D and 3D models,  
8 or images, of the resistivity distribution in the subsurface. Data collection and processing  
9 methodologies are widely described in the literature (e.g. Slater et al., 2002; Bentley and  
10 Gharibi, 2004; Cassiani et al., 2006), and so only a brief description is provided here. ERT  
11 surveys involve making a large number of four-point direct current (DC) electrical  
12 measurements (consisting of pairs of current and potential electrodes) using computer  
13 controlled automated measurement systems and multi-electrode arrays. These data are  
14 inverted to produce images of the subsurface; this is typically achieved by using regularized  
15 nonlinear least-squares algorithms (e.g. Loke and Barker, 1996) in which the forward  
16 problem is solved using either finite element or finite difference methods. ERT electrodes can  
17 be deployed either as surface or borehole arrays, or as a combination of the two. Cross-hole  
18 imaging was selected for this study to ensure that ERT image resolution was maintained with  
19 depth. The superior depth resolution that can be achieved using cross-hole relative to surface  
20 imaging is particularly important when characterizing and monitoring complex ground  
21 conditions and processes, where information is required at the scale of the heterogeneities.  
22 Cross-hole imaging, unlike surface array imaging, can potentially resolve layers that are in  
23 the order of tens of centimetres thick at depths of more than ten metres (e.g. Kemna et al.,  
24 2004).

---

1  
2  
3 2  
4  
5  
6 3 **2.1 Application to hydrogeophysical investigations**  
7  
8

9 4 The use of ERT as a ground imaging technique is based on the petrophysical  
10 relationships linking resistivity, hydrogeological and geological parameters (e.g. Revil et al.,  
11 5 1998; Lesmes and Friedman, 2005). The degree of fracturing, porosity, tortuosity,  
12 6 mineralogy, saturation, temperature and groundwater resistivity all affect the resistivity of  
13 7 subsurface materials, thereby providing the basis for using ERT for geological and  
14 8 hydrogeological investigations. The use of ERT for characterizing subsurface geology is well  
15 9 documented, with many examples of investigating unconsolidated saturated sediments (e.g.  
16 10 Kilner et al., 2005; Froese et al., 2005), such as those found at the research site detailed in  
17 11 this study. Generally, the major lithological effect on resistivity in these types of sediments is  
18 12 the proportion and type of clay minerals (Shevnin et al., 2007), with increasing clay content  
19 13 causing a decrease in resistivity. The close link between resistivity and many important  
20 14 hydrogeological parameters and properties has led to the increased use of ERT for  
21 15 hydrogeophysical investigations, where it has been used to study groundwater quality (Ogilvy  
22 16 et al., 2009), moisture content (Zhou et al., 2001) and in-situ remediation (Daily and Ramirez,  
23 17 1995). Of particular significance for hydrogeophysical investigations are the Archie  
24 18 equations (Archie, 1942) that link resistivity with pore fluid conductivity, saturation and  
25 19 porosity. When used in time-lapse mode ERT can provide spatial or volumetric information  
26 20 on changes in the subsurface, which, assuming a fixed geology, are usually related to changes  
27 21 in saturation (both water and non-wetting phase NAPLs), temperature, and the composition  
28 22 of the pore fluid. In some cases, quantitative estimates can be made of seepage velocities  
29 23 (Sandberg et al., 2002; Wilkinson et al., 2009), spatial moments (Binley et al., 2002; Singha  
30 24

---

1 and Gorelick, 2005; Looms et al., 2008), hydraulic conductivity (Binley et al., 2002), and  
2 tracer mass and concentration (Singha and Gorelick, 2006; Oldenborger et al., 2007; Deiana  
3 et al., 2007 & 2008).

## 4 **2.2 DNAPL contamination and bioremediation**

5       Examples of the use of ERT to detect and monitor DNAPL in the subsurface are  
6 relatively sparse and can be divided into controlled laboratory studies and those concerned  
7 with imaging historic DNAPL spills at contaminated field sites. Laboratory based ERT has  
8 invariably shown DNAPL contamination causes an increase in resistivity (Weller et al., 1996;  
9 Daily et al., 1998; Chambers et al., 2004); this is because DNAPLs are typically highly  
10 resistive (Lucius et al., 1992). ERT imaging of DNAPL contaminated sites is described by  
11 Daily and Ramirez (1995), Newmark et al. (1998), Goes and Meekes (2004) and Cardarelli  
12 and Di Filippo (2009). Daily and Ramirez (1995) used cross-hole ERT to monitor the  
13 electron donor injection at the TCE contaminated Savannah River Site, South Carolina, US.  
14 They successfully imaged the injection of methane as a metabolic carbon source, the  
15 distribution of which revealed preferential flow pathways within the saturated deposit.  
16 Electrical signatures associated with contamination were not identified in either the baseline  
17 or time-lapse images, instead the images were dominated by lithological variation and  
18 changes associated with gas injection respectively. Newmark et al. (1998) used time-lapse  
19 cross-hole ERT to monitor the pumping of TCE from the Hill Air Force Base, Utah, US.  
20 Removal of pooled DNAPL resulted in a reduction in formation resistivity due to its  
21 replacement by relatively low resistivity water. Goes and Meekes (2004) described two  
22 stand-alone (i.e. not time-lapse) cross-hole ERT field investigations at a perchloroethene  
23 (PCE), TCE and methyl chloride contaminated site in Utrecht and Drenthe in the  
24 Netherlands. Limited correlation between contamination and high resistivities was observed,  
25 but overlaps in the resistivity ranges of contaminated and uncontaminated materials at the site

---

1 introduced significant ambiguity into the interpretation of the data. Cardarelli and Di Filippo  
2 (2009) used a combination of surface based ERT and induced polarisation to study a site  
3 contaminated with chlorinated solvents, and detected geoelectrical signatures consistent with  
4 the presence of DNAPL. These studies, with the exception of Newmark et al. (1998)  
5 highlight the difficulties in detecting DNAPL using ERT. Both the laboratory and field based  
6 studies revealed that DNAPL residual saturation does not have a strong effect on resistivity,  
7 and in field conditions with the added complication of significant heterogeneity these effects  
8 are easily masked.

9       Most previous work describing the application of ERT to DNAPL contamination  
10 problems has not considered changes in resistivity resulting from chlorinated solvent  
11 degradation or the injection of biostimulation fluids into the subsurface. In the case of  
12 LNAPL contamination, breakdown products can significantly reduce the resistivity of the  
13 pore fluid around the contaminant (Sauck, 2000; Atekwana et al., 2005). Acworth (2001) has  
14 presented evidence to suggest that similar effects can be associated with chlorinated solvent  
15 contaminants. He identified a field example of low resistivity zones associated with free  
16 phase DNAPL that he interpreted as resulting from the release of chloride due to the  
17 biotransformation of chlorinated solvents. The biotransformation of chlorinated solvents,  
18 such as trichloroethene, involves the replacement of chlorine on the chlorinated ethene  
19 molecule by hydrogen (Vogel and McCarty, 1985). The reaction typically proceeds under  
20 reducing conditions, where the sequential dechlorination releases a chloride ion during the  
21 formation of degradation intermediates cis-DCE, vinyl chloride (VC) and ethene respectively.  
22 The injection of electron donor fluids, such as vegetable oil emulsion and lactate, can also  
23 have a measurable effect on resistivity due to altered pore fluid chemistry (Lane et al., 2006),  
24 and could, therefore, potentially be imaged using ERT. The current evidence base suggests  
25 that ERT is therefore likely to be more effective for monitoring changes in the distribution of

---

1 DNAPL breakdown products, electron donor and other amendment fluids, than in directly  
2 detecting changes in residual non-wetting phase saturation.

### 3 **3. FIELD SITE DESCRIPTION**

#### 4 **3.1 History**

5 The site, which is located in the East Midlands of the UK, has an industrial legacy  
6 stretching back to the early 1900s that includes chemicals manufacture and processing,  
7 energy generation and waste disposal. The study area is on a site formerly used for the  
8 production of monochloroacetic acid (MCA), which is a chemical intermediate for a range of  
9 pharmaceuticals and insecticides. MCA was produced by the reaction of chlorine with acetic  
10 acid and acetic anhydrite. TCE was used in a purification step after the primary reaction;  
11 consequently, large volumes of TCE were stored on the site. The plant operated from the mid  
12 1960s through to 1990. Since closure, the surface structures at the site have been demolished,  
13 the concrete hard standings have been crushed and replaced, and subsurface structures  
14 including the MCA sump have been removed (Figure 1). Several phases of intrusive  
15 investigation have been carried out at the site to establish the geology and the nature and  
16 extent of contamination.

#### 17 **3.2 Geology & Hydrogeology**

18 The generalized geology of the site (Figure 2) comprises made (or artificial) ground,  
19 underlain by Quaternary alluvium and river terrace gravels, below which is Triassic Mercia  
20 Mudstone Group bedrock (Lelliot et al., 2008). The made ground consists of gravel-sized  
21 particles of brick, concrete, quartzite and quartz, in a matrix of sand, silt and clay. Recorded  
22 made ground thickness varies from 0.6 to 2.8 m. The underlying alluvium is sub-divided into  
23 the upper alluvium, which is a silty clay with an average thickness of 0.9 m, and the lower  
24 alluvium, which is a clayey silty sand with an average thickness of 1 m. The alluvium

---

1 generally displays a fining upward sequence and is characterized by millimetre scale  
2 laminations. The lower alluvium is lithologically similar to sandy zones within the gravel,  
3 and in places the change from alluvium to gravels is gradational. The river terrace gravels are  
4 poorly sorted with variable proportions of clay, silt and sand, and have an average thickness  
5 of 2.7 m. The gravels contain fine grained horizons as well as bands of clean gravel. The  
6 weathered top surface of the mudstone bedrock ranges from 0.5 to 1.25 m in thickness; it  
7 consists of soft clay with an increasing proportion of mudstone lithorelicts with depth. The  
8 unweathered mudstone contains discontinuous silty and sandy patches.

9           Groundwater flow across the site is predominantly to the south-southwest. The water  
10 table is located within the made ground and alluvium at a depth of approximately 1 m below  
11 ground level. The lower alluvium and gravels appear to be in hydraulic continuity with one  
12 another and constitute a minor aquifer. Hydraulic testing has shown that the hydraulic  
13 conductivity ( $K$ ) of the lower alluvium is relatively uniform, with an average value of 10  
14 m/day, which is consistent with a sandy material with a relatively small proportion of silt and  
15 clay. The  $K$  of the gravels displays a very high spatial variability with recorded values  
16 ranging from 0.1 to 26 m/day, reflecting the strong heterogeneity observed during intrusive  
17 investigations.

### 18 **3.3 Contamination**

19           The principal contaminant at the site is TCE. Eyewitness accounts from former  
20 workers at the plant indicate that spillages and leaks occurred during the transfer of TCE to  
21 and from the holding tanks. Spills and waste, including TCE, were channelled through the  
22 drainage gully running through a washing plant floor into a sump and then into a trade  
23 effluent drain. No estimates of the total mass of DNAPL released into the sub-surface could  
24 be made based on historical records and accounts.

---

1 Site investigation has revealed a spatially variable distribution of chlorinated  
2 compounds in the groundwater and soil based on volatile organic compound (VOC)  
3 concentrations in groundwater, Sudan IV dye tests, and membrane interface probe results.  
4 This distribution was consistent with DNAPL release from the gully and sump associated  
5 with the MCA plant area. Most of the contamination has been identified within the gravels,  
6 and across the top of the mudstone, and in places has penetrated the mudstone through  
7 fractures. DNAPL is now primarily present at residual saturation with only limited small-  
8 scale pooling. Reductive dechlorination has occurred across much of the area as indicated by  
9 the transformation of TCE to cis-DCE, VC and ethene, and the presence of redox sensitive  
10 dechlorination indicators (e.g. dissolved oxygen and redox potential), which have been  
11 detected downstream of the gully and sump. Estimates of subsurface DNAPL mass in the  
12 vicinity of the MCA plant based on the site investigation range from 1 to 15 tonnes.

## 13 **4. METHOD**

### 14 *4.1 Experimental Design And Execution*

15 Detailed overviews of the wider experimental design are given by Zeeb et al. (2008)  
16 and Roberts et al. (2008). A brief outline of the experiment is given here, with particular  
17 reference to the geophysical objectives and monitoring approach.

18 The experiment was conducted within a contained in-situ test cell, which was  
19 separated from the rest of the site by plastic sheet piled walls that extended below the surface  
20 of the mudstone bedrock. The test cell isolated a portion of the DNAPL source and plume  
21 zone. The piles were designed to hydraulically isolate the aquifer in the cell and were located  
22 at a suitable distance from the transect electrodes such that they would not affect the  
23 resistivity data. Construction of the cell facilitated detailed performance monitoring, and

---

1 allowed for improved hydraulic control. In particular, the hydraulic gradient within the cell  
2 was increased, producing a mean residence time of 40 days, to achieve a more rapid  
3 reduction in DNAPL mass through increased dissolution during the experiment. The cell was  
4 30 m long, 4 m wide, and extended to an average depth of 6.2 m below ground level. The  
5 long axis of the cell was oriented approximately parallel to the prevailing groundwater flow  
6 direction. The influent end of the cell was not piled, thereby allowing groundwater from the  
7 site to flow into the cell; the influent end comprised a gravel pack trench containing fully  
8 screened wells for sample collection and amendment fluid injection. The effluent end was  
9 piled and a gravel pack abstraction trench containing fully screened wells was installed, from  
10 which groundwater was pumped at a rate of 1.4 litres per minute to maintain a hydraulic  
11 gradient of 0.022 within the cell.

12         ERT monitoring was carried out in two transects, each consisting of seven 100 mm  
13 diameter boreholes at lateral intervals of approximately 0.5 m, positioned in the source and  
14 plume zones respectively (Figure 1). Geological logs from these holes are shown in Figure 2;  
15 lithological interface positions are estimated where core loss, and associated slippage in the  
16 core barrels during drilling, occurs. Each of the holes extended to the mudstone bedrock, and  
17 was instrumented with multilevel sampler (MLS) arrays comprising 10 mm diameter access  
18 lines with ports at 0.5 m intervals with screen lengths of 100 mm, and ERT arrays with  
19 electrodes at 0.2 m intervals (Wilkinson et al., 2008). The boreholes were then left to collapse  
20 back around the installed arrays. Groundwater samples and subsequent chemical analyses  
21 from these provided control data for the geophysical monitoring, and a range of in-situ  
22 bioremediation performance metrics, including contaminant mass flux. The MLS and ERT  
23 arrays described here provided a level of resolution not seen in commercial applications and,  
24 along with Davis et al. (2009), represents one of the most detailed experimental designs to  
25 date for the monitoring of in-situ bioremediation.

---

1 Monitoring of the cell was divided into a 100 day baseline period prior to  
2 biostimulation (Days -100 to -1) and an operational period of 600 days that began  
3 immediately after the injection of the electron donor (Days 1 to 600). The electron donor used  
4 in this case was a vegetable oil based emulsion (Roberts et al., 2008). Between Days -6 and -  
5 2 a total of 2480 l of donor was injected into the cell using a total of 17 donor injection wells  
6 of 25 mm diameter were positioned in clusters of 2, 3 or 4 wells as shown in Figure 1. Each  
7 well was screened over a 1 m interval, either from 3-4 m (in clusters of 3 wells only), 4-5 m  
8 or 5-6 m to homogenise the distribution of EVO throughout the aquifer depth. During  
9 pressurised EVO injection, pumping from the equivalent well on the opposite side of the  
10 experimental cell enhanced lateral EVO coverage. At the time of injection the electron donor  
11 was diluted with groundwater to produce an average concentration of 5.05% by volume.  
12 Bioaugmentation with KB-1 bacteria was carried out between Days 13 and 14, with the  
13 injection of 60.6 l of fluid across the cell. During the early stages of the experiment monthly  
14 monitoring of the fully screened wells (Figure 1) indicated a decrease in pH to levels where  
15 reductive dechlorination of TCE would be significantly suppressed. Therefore, between Days  
16 111 and 248, sodium and potassium bicarbonate was continuously released into the influent  
17 trench wells at a rate averaging 7 g/minute, producing a concentration of 5 g/l.

18 Throughout the course of the experiment (during both the baseline and operational  
19 phases) groundwater sampling rounds generally took between one and two weeks, and so for  
20 convenience the timing of sampling events are described as having occurred on the middle  
21 day of the sampling round. Prior to sample collection, purging of the MLS arrays was carried  
22 out until steady state conditions were achieved; purge volumes averaged 3000 ml for each  
23 port. Purging and sample collection was carried out with a low flow pump (~20 ml/min), with  
24 the aim of producing a radial flow zone around the sample port. ERT measurements took  
25 approximately 7 hours for each transect. Baseline ERT measurements were performed during

---

1 the Day -25 monitoring event, and on Days 150, 240, 420, 510 and 600 of the operational  
2 phase of the experiment. Additional ERT measurements were performed on the source zone  
3 transect (SZT) on Day 1, immediately after the injection of electron donor.

4         The SZT and plume zone transect (PZT) were sampled for large suites of VOCs  
5 (including TCE, c-DCE, VC and ethene), anions, and cations, as well as sulphide, sulphate,  
6 alkalinity, electrical conductivity (EC) and total organic carbon (TOC). Sample analyses for  
7 VOC's and anions were carried out according to USEPA methods 5021a and 9056a (US  
8 EPA, 2007) respectively. Alkalinity and EC were measured at the well head using  
9 commercially available Hach Alkalinity Test kits and a Hanna HI9828 multiparameter probe.  
10 Immediately prior to the experiment during the baseline period, average concentrations of  
11 TCE, cDCE and VC within the SZT were 295, 501 and 50 mg/l respectively representing 27  
12 %, 63 % and 4.5 % of solubility (TCE: 1100 mg/l; cDCE: 800 mg/l VC: 1100 mg/l as per  
13 Fetter, 1999 and Lucius et al., 1992). Significant systematic variations in average anion  
14 concentrations within the transects were observed for bicarbonate and chloride in particular,  
15 and in pore fluid EC (Figure 3), which when corrected for temperature is controlled primarily  
16 by the concentration of dissolved ions. Variations in chloride, bicarbonate and hence pore  
17 fluid EC, are potentially significant drivers of bulk resistivity changes during the experiment;  
18 chloride was considered important as it is generated by the reductive dechlorination of TCE;  
19 bicarbonate was introduced into the cell in relatively high concentrations for pH control, and  
20 pore fluid EC is directly related to bulk resistivity (Archie, 1942). Sulphate was also present  
21 in elevated concentrations (i.e. hundreds of mg/l) within the cell due to transfer from the  
22 gypsum rich Mercia Mudstone bedrock, but was largely restricted to the base of the gravels,  
23 and did not display significant systematic variation during the experiment. Dissolved phase  
24 DNAPL molecules are not charged, and therefore do not significantly affect resistivity.  
25 Temperature also influences resistivity (e.g. Hayley et al., 2007), and should be considered in

---

1 seasonal monitoring experiments where air temperatures changes can cause substantial  
2 changes in ground temperatures. In this case, temperature records derived from the multilevel  
3 samplers during each of the monitoring rounds indicate that mean ground temperature  
4 variations below the water table ranged from 11 to 14.9 °C (Table 1), which assuming a 2 %  
5 change in resistivity per °C (Hayley et al., 2007), equates to a maximum bulk temperature  
6 induced resistivity change of approximately 8 %. Significant spatial trends in the temperature  
7 data were not apparent.

#### 8 ***4.2 ERT Data Acquisition, Processing And Inversion***

9 Apparent resistivity measurements were made on each panel (pair of boreholes) using an AGI  
10 SuperSting R8 IP system. This is a 200 W, eight-channel instrument, which permits the  
11 automated acquisition and storage of up to eight simultaneous apparent resistivity  
12 measurements for a given pair of current electrodes. A cross-hole measurement scheme was  
13 used (Figure 4) since this provides greater image resolution and better signal-to-noise  
14 characteristics than in-hole measurements (Bing and Greenhalgh, 2000). Current was passed  
15 between electrodes A and B, and potential differences were measured between adjacently  
16 numbered potential electrodes (i.e. P<sub>2</sub>-P<sub>1</sub>, P<sub>3</sub>-P<sub>2</sub>, ... , P<sub>9</sub>-P<sub>8</sub>). A and B were initially positioned  
17 near the base of each borehole, and were selected so that the A-B current bipole was as close  
18 to horizontal as possible given the differing vertical offsets of each hole. The eight  
19 subsequent cross-hole potential differences were measured, and then A was moved to the  
20 position of B, B to P<sub>1</sub>, P<sub>1</sub> to P<sub>2</sub> etc, and the process was repeated. This continued until the top  
21 of the boreholes was reached. At this point, a similar scheme was used where the potential  
22 differences below A and B were measured, with A and B moving back down the boreholes.  
23 This ensured that each measurement was made twice in reciprocal configurations, in which  
24 the electrodes forming the current and potential bipoles are interchanged. The Lorentz

---

1 reciprocity theorem implies that the apparent resistivity should be the same when measured in  
2 reciprocal configurations (Parasnis, 1988). Hence the average of a reciprocal pair of  
3 measurements was taken as the apparent resistivity for any given measurement configuration.  
4 The difference between the pair of measurements should ideally be zero. Any deviation from  
5 this gives a measure of the quality of the data, which is particularly effective for assessing  
6 errors due to high contact resistances, random errors arising from the resistivity instrument  
7 and sporadic errors due to background noise (Slater et al., 2000). Due to the location of the  
8 site, in an active industrial complex, the data were affected by noticeable levels of random  
9 noise. Therefore the differences between pairs of reciprocal measurements were used to  
10 weight the data in the inversion. The distribution of percentage reciprocal errors for the  
11 baseline data set is shown in Table 2. The percentage reciprocal error is given by  $100 (\rho_f - \rho_r)$   
12  $/ (\rho_f + \rho_r)$ , where  $\rho_f$  is the resistivity measurement, and  $\rho_r$  is its reciprocal. The mean  
13 reciprocal errors for each monitoring round are shown in Table 3.

14 The boreholes comprising the two transects were closely spaced, which led to a  
15 source of error that could not be accounted for by reciprocal measurements since it was  
16 systematic in nature. In a previous paper (Wilkinson et al., 2008), we demonstrated that  
17 measurements made on closely spaced boreholes can be prone to large systematic errors  
18 caused by uncertainties in the depths of the electrodes. Following the methods presented in  
19 that paper, we calculated an estimate of sensitivity to geometric error for each of the electrode  
20 configurations that were used. Any measurement with a relative sensitivity of  $>5.0 \text{ m}^{-1}$  (such  
21 that an uncertainty in depth of 0.01 m would lead to an error of  $>5\%$  in the apparent  
22 resistivity measurement) was discarded from the data set.

23 The baseline data for each transect were inverted using the Res2DInv software, with a finite-  
24 element method to permit the inclusion of topography, a Gauss-Newton solver, an  $L_2$   
25 (smoothness) model constraint, an  $L_1$  (robust) data constraint, and using logarithms of the

---

1 apparent resistivity data for stability (Loke et al., 2003). The  $L_1$  data constraint was chosen to  
2 reduce the effects of outlying data on the inverted model. The  $L_2$  model constraint was  
3 selected to better represent geological boundaries that were not necessarily aligned along  
4 model block edges; the compromise inherent in this choice being that the boundaries tend to  
5 become represented by gradational changes in resistivity. The method of active constraint  
6 balancing (Yi et al., 2003) was used, which increases the weight of the model constraint in  
7 regions where the sensitivity is low (see Figure 5). This approach helps to maximize spatial  
8 image resolution, whilst preserving inversion stability. Figure 5 shows that the sensitivity is  
9 strongly localized within 0.5 m of the limits of the SZT plane. This justifies the assumptions  
10 that 2.5D (i.e. 3D current flow in a 2D resistivity model) inversion can be used in this  
11 inherently heterogeneous environment and that the effect of the sheet piled walls on the data  
12 will be negligible (the PZT sensitivity distribution is not shown but is similar). The horizontal  
13 and vertical components of the model constraint were equally weighted throughout the model  
14 space due to significant heterogeneity being present in each direction. For each inversion, a  
15 homogeneous half-space was used as the initial model with resistivity equal to the average  
16 apparent resistivity (although the results were not found to be particularly sensitive to the  
17 choice of initial model). Subsequent data sets were inverted using time-lapse constraints to  
18 reduce image artefacts caused by noisy data (Loke, 2001). Each subsequent set was inverted  
19 in sequence, using the preceding inversion as an initial model and also as a reference model  
20 (i.e. the inversion of the monitoring d1 data used the inverted baseline model as a reference;  
21 the d150 data used the inverted d1 model as a reference; etc.). An  $L_1$  time-lapse constraint  
22 was imposed on the differences between the reference and the inverted models. This allowed  
23 resistivity changes with well defined boundaries, such as those associated with preferential  
24 transport pathways, to be imaged accurately. The inverted models were discretized on a grid  
25 with a vertical spacing of 0.2 m, and a variable horizontal spacing of  $(\Delta x_i / 9)$ , where  $\Delta x_i$  was

---

1 the spacing between the  $i$ th and  $(i + 1)$ th boreholes. This varied between 0.04 m and 0.09 m.  
2 The grid for the SZT comprised 1728 model blocks, and for the PZT, 1440 model blocks,  
3 whilst the data sets comprised 1851 apparent resistivity measurements for the SZT and 1463  
4 measurements for the PZT. It was found that three iterations were sufficient for each time-  
5 lapse image to converge.

## 6 **5. RESULTS & DISCUSSION**

### 7 *5.1 Baseline Resistivity Images*

8 Baseline resistivity sections are shown in Figure 6 (b and d). The area defined by the  
9 black masking at the top of the resistivity sections shows the extent of the unsaturated zone.  
10 Comparison with the geological logs in Figure 2 and the transect geology Figure 6 (a and c)  
11 reveals a clear correlation between resistivity and lithology. The gravels are the most resistive  
12 unit with values ranging from approximately 50 to 100  $\Omega\text{m}$ . Alluvium resistivities are  
13 generally lower with values in the range of 10 to 100  $\Omega\text{m}$ . The mudstone bedrock is generally  
14 characterized by resistivities of less than 50  $\Omega\text{m}$ . Comparison of the interface geometry,  
15 however, reveals significant differences between the borehole and ERT data. In particular,  
16 the gravel/mudstone interface in both transects was interpreted as being highly irregular from  
17 the borehole data, with vertical changes in elevation of up to 1 m of over horizontal distances  
18 on the order of 0.5 m. The ERT images show the bedrock surface as having a more gentle  
19 topography. Given that the interface geometry derived from the ERT sections are  
20 geologically more realistic, and the core recovery (see Figure 2) and slippage in the liner  
21 posed significant problems during drilling, it is probable that the bedrock surface is more  
22 regular than indicated by the borehole data alone.

23 The lithological similarities between the lower alluvium and the gravels, as  
24 determined from the site investigation, are reflected in the ERT images. The boundary

---

1 between these materials appears to be gradational. This is particularly apparent in the source  
2 SZT (Figure 6b) where there is no clear division between the alluvium and gravel.

3         The heterogeneity of the resistivity sections clearly reflects the geology of the site,  
4 which in the case of the gravels and alluvium is known to be complex and highly variable. In  
5 addition, some of the variability appears to be unrelated to geological features. Of particular  
6 note is the vertical banding associated with the borehole locations, where the region  
7 immediately surrounding the borehole is generally less resistive. In this case, the resistivity  
8 contrast in the disturbed zone around the boreholes is relatively modest (i.e. less than an order  
9 of magnitude) and so it is likely that the observed vertical banding is related to a real  
10 subsurface resistivity contrast rather than being an artefact of the inversion process (Nimmer  
11 et al. 2008). Further evidence of the reality of the banding is provided in Figure 7. This shows  
12 raw in-hole dipole-dipole apparent resistivity data that were not used in the inversion. The  
13 data were taken from the borehole at  $x = 2$  m on the SZT with a dipole length of  $a = 0.2$  m  
14 and interdipole spacings of  $na$  where  $n = 1-8$ . The raw data are shown as filled circles and the  
15 interpolating lines were calculated from linear interpolation of the raw data on a triangulated  
16 mesh. The data show that, independent of depth, the apparent resistivity tends to increase  
17 with small radial distances from the hole axis, reaching a maximum somewhere between  
18 0.15 m and 0.25 m. This exactly reflects the structure of the vertical banding seen in the  
19 resistivity sections. A probable cause of the banding is drill core removal and drilling  
20 disturbance. During drilling a 100 mm diameter core was removed from each borehole within  
21 the transects. The combined ERT and MLS arrays, with maximum and minimum diameters  
22 of the monitoring arrays were 63 mm and 37 mm respectively, were introduced into the  
23 holes, the casing was then removed allowing the holes to collapse. The total volume of pore  
24 or void space generated through the removal of borehole core, taking into account the  
25 introduction of the monitoring arrays, has been calculated to vary between 4750 and 6800

---

1 cm<sup>3</sup> per metre. This increase in water filled pore or void space will inevitably have caused a  
2 reduction in formation factor in the disturbed zones around the boreholes (particularly in the  
3 more resistive gravels), and hence the observed vertical banding. To support this  
4 interpretation we have modelled the effects of core removal and drilling disturbance in an  
5 otherwise homogeneous 3D resistivity distribution. A horizontal slice through this model is  
6 shown in Figure 8a. The background resistivity is taken to be 100 Ωm, whilst the removed  
7 core space and disturbed zones have resistivities of 10 Ωm and 30 Ωm respectively. The  
8 geometry of the model is also simplified, with the boreholes spaced at 0.5 m and no vertical  
9 offsets between the boreholes. Despite the simplicity, the inversion of simulated crosshole  
10 data from this model exhibits vertical banding that is very similar in physical extent and  
11 resistivity contrast to that observed in the transect images (Figure 8b).

12 As anticipated, DNAPL was not detected in the baseline images, as the effects of  
13 residual DNAPL contamination could not be separated from the more dominant signatures of  
14 the lithological variability and drilling disturbance. This finding is consistent with Daily and  
15 Ramirez (1995) and Goes and Meeke (2004) who found that residual contamination was  
16 difficult to detect from baseline ERT images.

## 17 ***5.2 Time-Lapse Resistivity Images***

18 Time-lapse resistivity images for the SZT and PZT are shown in Figure 9 and Figure  
19 10 respectively. The data are presented as both resistivity models for each time interval and  
20 normalized resistivity images that are calculated as the resistivity ratio of the time-lapse and  
21 baseline models. Resistivity ratios of less than 1 represent a decrease in resistivity relative to  
22 baseline conditions, whilst values of greater than 1 indicate an increase in resistivity. The  
23 variability in water levels during the experiment was due to a combination of intermittent  
24 faults with the abstraction pumps and pore clogging in the influent trench causing reduced

---

1 flow into the cell. The mean misfit errors between the measured and inverted data are also  
2 shown in the upper right-hand corner of each image. These are consistent with the observed  
3 levels of random (i.e. reciprocal) and systematic (i.e. geometric) error in the data, which were  
4 approximately 3% and 5% respectively.

5         The ERT time-series for both transects contain broadly similar features. The most  
6 significant change is the appearance of a low resistivity zone towards the base of the gravels  
7 at approximately 35 m above Ordnance Datum (AOD). In the SZT it is a well defined feature  
8 that is concentrated on the right hand side of the cell between  $x = 1$  and 2.7 m, which appears  
9 by Day 1, strengthens considerably by Day 150, peaks at Day 240 and persists to the end of  
10 the experiment at Day 600. In the PZT the feature is slightly more diffuse, but extends across  
11 the entire width of the section. Again, it peaks at Day 240 and persists for the remainder of  
12 the experiment.

13         The influence of temperature is not readily apparent from the time-lapse resistivity  
14 sections, and is not considered to have significantly affected this experiment. The reasons for  
15 this are twofold. First, the observed temperatures changes are likely to have caused relatively  
16 small changes in resistivity, similar in magnitude to data error and model misfit errors,  
17 compared to the large changes in bulk resistivity changes shown in the resistivity ratio plots.  
18 Second, temperature fluctuations will have produce broad changes in resistivity, diminishing  
19 with depth, whereas the major changes observed from the monitoring data are localized and  
20 concentrated towards the base of the transects.

### 21 *5.2.1 Electron Donor Injection*

22         The magnitude of the observed resistivity changes in the SZT and the PZT are  
23 indicated in Figure 11, where the average resistivity changes within the low resistivity  
24 regions towards the base of the gravels (see dotted boxes in Figure 9 and Figure 10) are

---

1 plotted. For the SZT a drop in resistivity of approximately 30 % is observed between the  
2 baseline and Day 1 resistivity sections. The major change to cell during this period was the  
3 introduction of electron donor, which has caused the decrease in resistivity. Although this  
4 drop in resistivity is apparent in Figure 9, it is clear that the electron donor has not produced  
5 the level of resistivity contrasts seen later in the experiment (i.e. Days 150 to 600 - Figure 9).  
6 A smaller resistivity ratio range, as shown in Figure 12, is therefore required to see the  
7 relevant detail in the Day 1 image. The localized nature of the resistivity decrease indicates  
8 that the electron donor has exploited a preferential pathway within the gravels. The location  
9 of the inferred preferential pathway is coincident with a coarse zone of gravel identified from  
10 particle size distribution analysis of core samples recovered from the SZT. The significant  
11 drop in resistivity associated with the electron donor injection is due to the soluble  
12 components, which include 2.4 % sodium lactate and other soluble nutrients. The electrical  
13 conductivity of electron donor concentrate is 7200  $\mu\text{S}/\text{cm}$ . Due to its strong electrical  
14 signature, ERT proved to be an effective means of mapping the spatial distribution of the  
15 electron donor within a highly heterogeneous deposit. This finding parallels that of Daily and  
16 Ramirez (1995), who used the injection of an electrically insulating gas (methane electron  
17 donor and air mix), rather than an electrically conductive emulsion, to map preferential flow  
18 pathways in a TCE source zone. The relative lack of change around the boreholes may be  
19 due to the dilution of high EC fluids within the zones of increased porosity around the  
20 boreholes, or due to inversion artefacts related to the spatially variable sensitivity of the  
21 acquisition scheme.

### 22 *5.2.2 Bicarbonate Buffer Injection*

23 The continued decrease in bulk resistivity on Days 150 and 240 is a function of  
24 bicarbonate buffer injection. In the influent trench groundwater the EC averaged 800  $\mu\text{S}/\text{cm}$   
25 from the start of baseline monitoring to the injection of bicarbonate on Day 111. During

---

1 bicarbonate injection the average EC increased to 9000  $\mu\text{S}/\text{cm}$ , and after injection gradually  
2 decreased to 1600  $\mu\text{S}/\text{cm}$  by Day 600. The increase in bicarbonate and the corresponding rise  
3 in EC (which is the inverse of resistivity) observed from the MLS arrays (Figure 13 and  
4 Figure 14), reflects the trend seen in the influent trench. The concentration of bicarbonate and  
5 EC levels are higher in the SZT than the PZT due to dilution and dispersion of bicarbonate  
6 along the cell. This is also evident from the ERT sections where the low resistivity feature is  
7 stronger in the SZT (Figure 9) than in the PZT (Figure 10).

8         The spatial distribution of the alkalinity and EC determined from the MLS arrays are  
9 shown in Figure 13 and Figure 14. High alkalinities from Day 150 in the SZT and PZT are  
10 concentrated towards the base of the gravels in positions broadly similar to the low resistivity  
11 anomalies that have been identified as preferential flow pathways. Spatial averaging of ERT  
12 derived resistivity and measured alkalinity within this area has revealed a strong correlation  
13 between the two (Figure 15c), indicating that alkalinity is the dominant driver of resistivity  
14 changes. The primary differences between the ERT images and the alkalinity and EC MLS  
15 plots are the diffuse nature of the MLS plots, compared to the corresponding features seen in  
16 the resistivity sections. The reasons for this are likely to be twofold. Firstly, the spatial  
17 resolution achievable from the ERT arrays is higher than that from the MLS arrays. The MLS  
18 ports were distributed on a 0.5 m grid within the transect, i.e. located in boreholes separated  
19 by approximately 0.5 m, and positioned at 0.5 m depth intervals within these boreholes. This  
20 produces an effective sampling area of 0.5 x 0.5 m for each port within the plane of the  
21 transect. The resolution of the ERT is a function of number of factors including mesh  
22 discretization, electrode geometry, measurement configurations and data quality. In this case  
23 with good data quality, vertical and horizontal electrode separations of 0.2 m and 0.5 m  
24 respectively, and the number of measured data exceeding the number of model cells, it is  
25 likely that model resolution will approach that of the chosen mesh discretization, i.e. 0.2 x

---

1 0.05 m. The resolving capabilities of the MLS arrays was also affected by incomplete  
2 recovery of samples from the transects. During some monitoring rounds samples could not be  
3 collected from a number of ports due to low flow rates (assumed to result from clogging of  
4 the well screen) and drawdown of the water table that led to partially saturated conditions in  
5 some of the upper sampling ports; port locations used for the respective sampling rounds are  
6 marked on Figure 13 and Figure 14 as grey dots. Secondly, the disturbed zones around the  
7 boreholes, the presence of voids caused by the incomplete collapse of the boreholes, and void  
8 space within the stem of the MLS and ERT arrays will have produced preferential  
9 groundwater flow pathways along the boreholes. These higher permeability zones, coupled  
10 with the purge volumes that were required to achieve steady state hydrochemical conditions,  
11 are likely to have affected sample collection from the MLS ports. Evidence for this is seen  
12 particularly in the SZT, where vertical banding is apparent in the MLS plots (e.g. Figure 13a -  
13 Day 240, Day 510; Figure 13c – Day 510). The disturbed zone also appears to have allowed  
14 the sinking of denser electrically conductive groundwater towards the lower sections of the  
15 boreholes in a similar manner to that described by Kuras et al. (2009), during an experiment  
16 using cross hole ERT to monitor saline tracer migration. The hypothesis is supported by the  
17 observed distribution of EC changes in both the SZT and PZT plots, where there is a lack of a  
18 distinct lower interface for the higher EC zones (e.g. Figure 13a and Figure 14a), whereas the  
19 top interfaces are generally better defined and more consistent with the high EC (or low  
20 resistivity) features seen in the normalized ERT images (Figure 9 and Figure 10). The diffuse  
21 nature of the MLS plots is also due to the lack of samples (locations shown as grey dots); this  
22 is a particular problem towards the base of the sections, and has in a number of cases resulted  
23 in the extrapolation of high EC and concentration values into the bedrock (e.g. Figure 13a  
24 and b, day 240). Although borehole disturbance appears to have affected groundwater  
25 sampling, the vertical variations in groundwater composition that are observed within the

---

1 MLS arrays indicate that a significant component of the collected pore water was from  
2 undisturbed formations.

### 3 5.2.3 Chloride

4 The MLS results from the PZT show that reductive dechlorination is occurring in the  
5 cell, as evidenced by a decrease in TCE levels and an increase in c-DCE and VC (Figure 3).  
6 Within the preferential flow pathway defined in the SZT and PZT, average chloride levels  
7 varied by approximately 300 and 400 mg/l respectively during the course of the experiment  
8 (Figure 13c and Figure 14c). The main driver for this change is likely to be reductive  
9 chlorination. No other known significant sources of chloride were introduced into the cell  
10 during this time; in particular, the chloride content of the electron donor concentrate was low  
11 (i.e. ~50 mg/l). This magnitude of change (i.e. several hundred mg/l) would have had a  
12 significant impact on pore fluid EC, and hence, bulk resistivity. For example, a change even  
13 at high chloride concentrations of 1200 to 1600 mg/l, in a solution of sodium chloride, will  
14 produce a corresponding change in EC from 5000 to 6600  $\mu\text{S}/\text{cm}$  (Weast, 1986), equivalent  
15 to a change in fluid resistivity of 24%. However, the consequence of using the bicarbonate  
16 buffer for the ERT monitoring is that it has significantly altered the groundwater resistivity in  
17 the cell, which has served to obscure the more subtle affects of chloride release from the  
18 reductive dechlorination of TCE. Evidence for the detection of chloride level fluctuations by  
19 the ERT monitoring is therefore limited. Figure 15a and b shows average changes in bulk  
20 resistivity in the ERT sections towards the base of the gravels (dashed boxes – Figure 9 and  
21 Figure 10) plotted against average pore fluid EC, alkalinity and chloride concentrations from  
22 MLS ports in the same area. Bulk and pore fluid resistivity (or EC) measurements would be  
23 expected to follow similar trends; this is observed in the data, with the exception of day 240  
24 in the SZT and day 510 in both the SZT and PZT where pore fluid resistivities are maintained  
25 at higher levels relative to the bulk resistivity values. Although the increase in alkalinity from

---

1 baseline to Day 240 is similar in the resistivity data, the decrease in alkalinity after Day 240  
2 is not accompanied by an equivalent increase in resistivity. At this point, bulk and pore fluid  
3 resistivity increases are smaller than would be predicted if alkalinity were the sole driver of  
4 resistivity changes, which may indicate that chloride is maintaining the resistivity at lower  
5 levels; this is particularly apparent in the SZT (Figure 15a) in both the bulk and pore fluid  
6 resistivity data. However, given the evidence of preferential flow within the disturbed zone  
7 around the boreholes during groundwater sampling, and the differences between the average  
8 bulk and pore fluid resistivity values, this interpretation is necessarily tentative.

#### 9 *5.2.4 Comparison of ERT, Falling Head Tests and Bromide Tracer Test Results*

10 The regions of low resistivity associated with high concentrations of electron donor  
11 and bicarbonate form discrete layers towards the base of the gravels. This is good evidence  
12 for a high permeability preferential pathway in this area. This hypothesis has been supported  
13 by further hydraulic testing at the site including a bromide tracer test, described by Dearden  
14 et al. (2010), which was monitored in the SZT, and falling head slug tests, which were  
15 performed on both the SZT and the PZT. Falling-head tests (Chirlin, 2007), which involved  
16 adding water to a monitoring well to create an instantaneous head change, were used here to  
17 measure hydraulic conductivity. The rate of recovery of the change in water level is a  
18 function of the hydraulic properties of the aquifer adjacent to the well (Pandit and Miner,  
19 1986). The resulting head decay was interpreted here using an equation from Hvorslev  
20 (1951) that accounts for the specific geometry of the well completion. The bromide tracer  
21 was released into wells IW1, IW2 and IW3 (Figure 1), which were screened within the river  
22 terrace deposits, between 1.3 and 5.3 m below ground level. The spatial variation of the  
23 average tracer concentration recovered over 24 days is shown in Figure 16a. Hydraulic  
24 conductivity values determined from the falling head tests are shown in Figure 16b and  
25 Figure 16d. Differences between the ERT and MLS based results will be a function of the

---

1 differing spatial resolution of the techniques, noise effecting the ERT data, and the effect of  
2 the disturbed zone on measured  $K$  values (e.g. Butler, 2005).

3 Estimation of hydraulic conductivity,  $K$ , directly from resistivity is not possible  
4 because the contributions of pore fluid conductivity and interfacial conductivity, which are  
5 linked to pore volume and pore surface area respectively, cannot be separated (e.g. Slater,  
6 2007). This is particularly true in complex field situations such as this, where the proportion  
7 of clay, and hence the contribution of mineral surface conduction, varies considerably and is  
8 not well constrained by ground truth data. Moreover, the indirect determination of  $K$  using  
9 groundwater velocities derived from time-lapse ERT (e.g. Binley et al., 2002) was not  
10 possible in this study because the temporal resolution of the ERT monitoring was insufficient  
11 to capture the bicarbonate breakthrough characteristics. Also, ERT could not be used as a  
12 monitoring tool for the tracer test as bromide concentrations were too low to be detected.  
13 Instead, we use correlation coefficients to assess the similarity between the spatial  
14 distributions of the resistivity changes and the average bromide concentration  $\bar{c}$  or  $K$ . We  
15 define the spatial correlation coefficient,  $r$ , as

$$r = \frac{\iint_S p \log\left(\frac{\rho}{\rho_b}\right) dS}{\sqrt{\iint_S p^2 dS \iint_S \log^2\left(\frac{\rho}{\rho_b}\right) dS}},$$

17 where  $p$  stands for either  $\bar{c}$  or  $K$ , and  $S$  is the region bounded by the outer boreholes of the  
18 transect over the depth interval 33.5 m - 37 m AOD.

19 To interpret  $r$ , we note that Schwarz's Inequality guarantees that  $-1 \leq r \leq 1$ . We also  
20 note that  $\bar{c}$  and  $K$  are  $\geq 0$  everywhere, and that  $\log(\rho/\rho_b) < 0$  for regions that have become  
21 more electrically conductive than the baseline and  $> 0$  for regions that have become more  
22 resistive. So therefore we would expect  $r$  to be significantly  $< 0$  if the distributions of  $\bar{c}$  or  $K$   
23 are predominantly similar to regions that have become more electrically conductive, or

---

1 significantly  $> 0$  if they are similar to regions that have become more resistive. If there was  
2 no overall correspondence, we would expect  $r \approx 0$ .

3 For the average bromide concentration  $\bar{c}$  observed on the SZT (Figure 16a), we find  $r$   
4 = -0.62, and for the hydraulic conductivity  $K$  (Figure 16b), we find  $r = -0.58$ . These values  
5 show that the regions of higher  $\bar{c}$  and  $K$  correlate well with the regions where electrical  
6 conductivity increased, supporting the interpretation that the ERT monitoring of the  
7 bicarbonate transport did indeed highlight preferential flow pathways. If we remove the  
8 region surrounded by the dashed line in Figure 16b from the calculation, we find that the  
9 coefficient for  $K$  increases to  $r = -0.68$ . This is reasonable to do, since very little tracer was  
10 recovered in this region, indicating that whilst a localized high  $K$  zone is present the majority  
11 of the tracer mass was focused on the lower right-hand-side of the cell.

12 Similarly, we can calculate the correlation coefficient between the hydraulic  
13 conductivity (Figure 16d) and the resistivity changes (Figure 16e) for the PZT. We find that  $r$   
14 = -0.72, again showing a strong correlation between hydraulic conductivity and regions of  
15 increased electrical conductivity. These quantitative results support the qualitative  
16 observation that the regions of high  $\bar{c}$  and  $K$  look similar to the regions where the bicarbonate  
17 increased the electrical conductivity, and strengthens the argument that the ERT monitoring  
18 revealed preferential transport pathways.

19 The results of the ERT, indicating a major preferential flow pathway in the gravels,  
20 has significant implications for the distribution of DNAPL in the cell and the efficacy of the  
21 electron donor and KB-1 for bioremediation. The relatively high groundwater velocities in  
22 the preferential pathway appear to have depleted contaminant concentrations in this area of  
23 the SZT, as indicated by the relatively low concentrations of chloride, TCE and DCE  
24 observed within the pathway during the baseline monitoring phase (Figure 13). Conversely,

---

1 the distribution of TCE and its daughter products in the PZT are limited to the region of high  
2 permeability zone (Figure 14) indicating that the dissolved phase DNAPL from the source  
3 zone is being channelled almost exclusively along the preferential flow pathway.  
4 Consequently, it is likely that the delivery of electron donor and KB-1 to free phase DNAPL  
5 in the source zone was limited by the inaccessibility of the remaining contaminant, whilst in  
6 the plume zone delivery would have been more favourable.

## 7 **6. SUMMARY & CONCLUSIONS**

8 Baseline ERT images were an effective means of determining the geometry of the  
9 interface between the gravel aquifer and the underlying mudstone, in contrast to ambiguities  
10 in the interpretation of the borehole logs due to core loss and slippage. For sites with  
11 significant areas of pooled DNAPL, ERT has a clear role to play in the characterization of the  
12 surface topography of aquitards, which can control pooling and lateral migration. ERT  
13 provided evidence of the ground disturbance associated with drilling, although these effects  
14 were difficult to separate from possible data acquisition and inversion footprints .

15 The great strength of ERT is that it can see through the disturbed zone into pristine  
16 formation, whereas samples collected from MLS arrays can be influenced by the drilling  
17 disturbance and flow heterogeneity resulting from the collapse of boreholes as indicated by  
18 the vertical banding in some of the EC and concentration plots, and the diffuse nature of the  
19 features within these plots. This highlights the benefits of combined ERT and MLS  
20 monitoring approaches, for which high resolution spatial data generated from geoelectrical  
21 imaging can aid in the interpretation of groundwater sampling data. However, interpretation  
22 of these data sets must take into account possible ERT data acquisition artefacts and  
23 preferential sampling of the disturbed zone during groundwater sampling.

---

1 Crucially, ERT imaging has proved effective as a means of spatially imaging the  
2 subsurface distribution of the biostimulation and pH control fluids, thereby providing an  
3 important indicator of the performance of the substrate delivery process. Despite significant  
4 resistivity changes caused by biostimulation and pH control fluids introduced into the cell, a  
5 resistivity signature consistent with changes in chloride levels was observed in both the SZT  
6 and PZT between Days 420 and 600, thereby providing tentative evidence that ERT may  
7 have detected a product of chlorinated solvent biodegradation.

8 The distribution of both the electron donor and bicarbonate determined from ERT  
9 provided strong evidence of a major preferential pathway in the cell. This finding was  
10 confirmed by subsequent tracer and falling head tests; the geometry of the preferential  
11 pathways identified from the ERT was shown to correlate well with the distribution of peak  
12 tracer concentrations and high  $K$  values determined from the falling head tests. The control  
13 exerted by preferential flow pathways on the distribution of contaminant and the delivery of  
14 biostimulation fluids has clear implications for the outcome of the bioremediation process,  
15 and further highlights the benefits of hydrogeophysical monitoring approaches that can  
16 achieve a level of spatial resolution closer to that of the scale of hydrogeological  
17 heterogeneity.

18 Most future attempts to monitor the progress of DNAPL bioremediation are unlikely  
19 to have the benefit of very closely spaced boreholes and a contained cell. Conventional site  
20 investigation and monitoring approaches rely upon more widely spaced boreholes, and more  
21 limited groundwater sampling. In such situations the use of ERT is likely to be even more  
22 advantageous. This is because high resolution imaging of geological and hydrogeological  
23 heterogeneity can still be achieved using borehole separations that are far less favourable than  
24 those used in this study (LaBreque et al., 1996), and recent advances in ERT monitoring

---

1 technology (e.g. Ogilvy et al., 2009) will allow for datasets to be collected at much higher  
2 temporal resolutions (i.e. at intervals of hours or days, rather than weeks or months).

### 3 **7. ACKNOWLEDGEMENTS**

4 This paper is published with the permission of the Executive Director of the British  
5 Geological Survey (NERC). The work was carried out as part of the SABRE (Source Area in  
6 situ BioREmediation) project, which was funded via the UK Bioremediation LINK  
7 Programme, receiving in-kind and direct financial contributions from each participating  
8 organization and financial contributions from BBSRC, DTI, the Environment Agency,  
9 EPSRC, and NERC. Work on SABRE at the British Geological Survey was supported by  
10 NERC (Grant No. NE/C513193/1).

### 11 **8. REFERENCES**

- 12 Acworth, R. I. (2001), Physical and chemical properties of a DNAPL contaminated zone in a  
13 sand aquifer, *Quarterly Journal of Engineering Geology and Hydrogeology*, 34, 85-98.
- 14 Ajo-Franklin, J. B., J. T. Geller, and J. M. Harris (2006), A survey of the geophysical  
15 properties of chlorinated DNAPLs, *Journal of Applied Geophysics*, 59(3), 177-189.
- 16 Archie, G. E. (1942), The electrical resistivity log as an aid in determining some reservoir  
17 characteristics, *Transactions of the AIME*, 146, 54-62.
- 18 Atekwana, E. A., E. Atekwana, F. D. Legall, and R. V. Krishnamurthy (2005),  
19 Biodegradation and mineral weathering controls on bulk electrical conductivity in a shallow  
20 hydrocarbon contaminated aquifer, *Journal of Contaminant Hydrology*, 80(3-4), 149-167.
- 21 Bentley, L. R., and M. Gharibi (2004), Two- and three-dimensional electrical resistivity  
22 imaging at a heterogeneous remediation site, *Geophysics*, 69(3), 674-680.

1  
2  
3  
4  
5  
6  
7  
8  
9  
10  
11  
12  
13  
14  
15  
16  
17  
18  
19  
20  
21  
22  
23  
24  
25  
26  
27  
28  
29  
30  
31  
32  
33  
34  
35  
36  
37  
38  
39  
40  
41  
42  
43  
44  
45  
46  
47  
48  
49  
50  
51  
52  
53  
54  
55  
56  
57  
58  
59  
60  
61  
62  
63  
64  
65

---

1 Bing, Z, and S. A. Greenhalgh (2000), Cross-hole resistivity tomography using different  
2 electrode configurations, *Geophysical Prospecting*, 48(5), 887-912.

3 Binley, A., G. Cassiani, R. Middleton, and P. Winship (2002), Vadose zone flow model  
4 parameterisation using cross-borehole radar and resistivity imaging, *Journal of Hydrology*,  
5 267(3-4), 147-159.

6 Brusseau, M. L., N. T. Nelson, Z. Zhang, J. E. Blue, J. Rohrer, and T. Allen (2007), Source-  
7 zone characterization of a chlorinated-solvent contaminated Superfund site in Tucson, AZ,  
8 *Journal of Contaminant Hydrology*, 90(1-2), 21-40.

9 Butler, J. J. (2005), Hydrogeological methods for estimation of hydraulic conductivity, in  
10 *Hydrogeophysics*, edited by Y. Rubin and S. Hubbard, pp. 23–58, Springer, The Netherlands.

11 Cardarelli, E. and G. Di Filippo (2009), Electrical resistivity and induced polarization  
12 tomography in identifying the plume of chlorinated hydrocarbons in sedimentary  
13 formation: A case study in Rho (Milan - Italy), *Waste Management & Research*, 27 (6), 595-  
14 602.

15 Cassiani, G., V. Bruno, A. Villa, N. Fusi, and A. M. Binley (2006), A saline trace test  
16 monitored via time-lapse surface electrical resistivity tomography, *Journal of Applied*  
17 *Geophysics*, 59(3), 244-259.

18 Chambers, J. E., M. H. Loke, R. D. Ogilvy, and P. I. Meldrum (2004), Noninvasive  
19 monitoring of DNAPL migration through a saturated porous medium using electrical  
20 impedance tomography, *Journal of Contaminant Hydrology*, 68(1-2), 1-22.

21 Chirlin, G. (2007), A critique of the Hvorslev method for slug test analysis: the fully  
22 penetrating well. *Ground Water Monitoring & Remediation*, 9(2), 130-138.

1  
2  
3  
4  
5  
6  
7  
8  
9  
10  
11  
12  
13  
14  
15  
16  
17  
18  
19  
20  
21  
22  
23  
24  
25  
26  
27  
28  
29  
30  
31  
32  
33  
34  
35  
36  
37  
38  
39  
40  
41  
42  
43  
44  
45  
46  
47  
48  
49  
50  
51  
52  
53  
54  
55  
56  
57  
58  
59  
60  
61  
62  
63  
64  
65

---

1 Daily, W., and A. Ramirez (1995), Electrical resistance tomography during in-situ  
2 trichloroethylene remediation at the Savannah River Site, *Journal of Applied Geophysics*,  
3 33(4), 239-249.

4 Daily, W., A. Ramirez, and R. Johnson (1998), Electrical impedance tomography of a  
5 perchloroethylene release, *Journal of Environmental and Engineering Geophysics*, 2(3), 189-  
6 201.

7 Davis, G.B., B.M. Patterson and C.D. Johnston (2009), Aerobic bioremediation of 1,2  
8 dichloroethane and vinyl chloride at field scale, *Journal of Contaminant Hydrology*, 107(1-  
9 2), 91-100.

10 Dearden, R., G. P. Wealthall, J. E. Chambers and M. Rivett (2010), Forced gradient  
11 conservative tracer test in the SABRE research cell. British Geological Survey,  
12 Commissioned Report CR/09/054, Nottingham, UK.

13 Deiana R., G. Cassiani, A. Villa, A. Bagliani and V. Bruno (2008), Model calibration of a  
14 water injection test in the vadose zone of the Po River plain using GPR cross-hole data, doi:  
15 10.2136/vzj2006.0137 *Vadose Zone Journal*, Feb 25 2008: 215-226.

16 Deiana R., G. Cassiani, A. Kemna, A. Villa, V. Bruno and A. Bagliani (2007), An  
17 experiment of non invasive characterization of the vadose zone via water injection and cross-  
18 hole time-lapse geophysical monitoring, *Near Surface Geophysics*, 5, 183-194.

19 Fetter, C. W. (1999), *Contaminant hydrogeology*, 2nd Ed. Prentice Hall: New Jersey, pp 500.

20 Froese, D. G., D. G. Smith, and D. T. Clement (2005), Characterizing large river history with  
21 shallow geophysics: Middle Yukon River, Yukon Territory and Alaska, *Geomorphology*,  
22 67(3-4), 391-406.

---

1 Goes, B. J. M., and J. A. C. Meekes (2004), An effective electrode configuration for the  
2 detection of DNAPLs with electrical resistivity tomography, *Journal of Environmental and*  
3 *Engineering Geophysics*, 9(3), 127-141.

4 Hayley, K., L.R. Bentley, M. Gharibi and M. Nightingale (2007), Low temperature  
5 dependence of electrical resistivity: Implications for near surface geophysical monitoring.  
6 *Geophysical Research Letters*, 34, L18402.

7 Hubbard, S. S., K. Williams, M. E. Conrad, B. Faybishenko, J. Peterson, J. S. Chen, P. Long,  
8 and T. Hazen (2008), Geophysical monitoring of hydrological and biogeochemical  
9 transformations associated with Cr(VI) bioremediation, *Environmental Science &*  
10 *Technology*, 42(10), 3757-3765.

11 Hvorslev, M. J. (1951) Time Lag and Soil Permeability in Ground Water Observations.  
12 Bulletin 36. U.S. Army corps of Engineers, Waterways Experimental Station, Vicksburg,  
13 Mississippi, 50 pp.

14 ITRC (Interstate Technology & Regulatory Council) (2007), In Situ Bioremediation of  
15 Chlorinated Ethene DNAPL Source Zones: Case Studies, Interstate Technology &  
16 Regulatory Council, Washington, D.C.

17 Kavanaugh, M. C., P. S. C. Rao, L. Abriola, C. Newell, J. Cherry, T. Sale, G. Destouni, S.  
18 Shoemaker, R. Falta, R. Siegrist, D. Major, G. Teutsch, J. Mercer, and K. Udell (2003), The  
19 DNAPL Remediation Challenge: Is There a Case for Source Depletion?, US Environmental  
20 Protection Agency, Washington, DC.

21 Kemna, A., A. Binley and L. Slater (2004), Crosshole IP imaging for engineering and  
22 environmental applications, *Geophysics*, 69(1), 97-107.

- 
- 1 Kilner, M., L. J. West, and T. Murray (2005), Characterisation of glacial sediments using  
2 geophysical methods for groundwater source protection, *Journal of Applied Geophysics*,  
3 57(4), 293.
- 4 Kueper, B. H., G. P. Wealthall, J. W. N. Smith, S. A. Leharne, and D. N. Lerner (2003), *An*  
5 *illustrated handbook of DNAPL transport and fate in the subsurface*, 63 pp., Environment  
6 Agency, Almondsbury, Bristol.
- 7 Kuras, O., J. Pritchard, P. I. Meldrum, J. E. Chambers, P. B. Wilkinson, R. D. Ogilvy, and W.  
8 G. P. Wealthall (2009), Monitoring hydraulic processes with Automated time-Lapse  
9 Electrical Resistivity Tomography (ALERT), *Comptes Rendus Geosciences*, 341, 868-885.
- 10 LaBrecque, D. J., A. L. Ramirez, W. D. Daily, A. M. Binley, and S. A. Schima (1996), ERT  
11 monitoring on environmental remediation processes, *Measurement Science & Technology*,  
12 7(3), 375-383.
- 13 Lane, J. W., F. D. Day-Lewis, and C. C. Casey (2006), Geophysical monitoring of a field-  
14 scale biostimulation pilot project, *Ground Water*, 44(3), 430-443.
- 15 Lane, J. W., F. D. Day-Lewis, R. J. Versteeg, and C. C. Casey (2004), Object-based inversion  
16 of crosswell radar tomography data to monitor vegetable oil injection experiments: *Journal of*  
17 *Environmental & Engineering Geophysics*, 9 (2), 63-77.
- 18 Lelliot, M. R., M. R. Cave and G. P. Wealthall (2008), A structured approach to the  
19 measurement of uncertainty in 3D geological models. *Quarterly Journal of Engineering*  
20 *Geology and Hydrogeology*, 42 (1), 95-105.
- 21 Lesmes, D. P., and S. P. Friedman (2005), Relationships between the electrical and  
22 hydrogeological properties of rocks and soils, in *Hydrogeophysics*, edited by Y. Rubin and S.  
23 Hubbard, pp. 87–128, Springer, The Netherlands.

1  
2  
3  
4  
5  
6  
7  
8  
9  
10  
11  
12  
13  
14  
15  
16  
17  
18  
19  
20  
21  
22  
23  
24  
25  
26  
27  
28  
29  
30  
31  
32  
33  
34  
35  
36  
37  
38  
39  
40  
41  
42  
43  
44  
45  
46  
47  
48  
49  
50  
51  
52  
53  
54  
55  
56  
57  
58  
59  
60  
61  
62  
63  
64  
65

---

1 Loke, M. H., and R. D. Barker (1996), Rapid least-squares inversion of apparent resistivity  
2 pseudosections by a quasi-Newton method, *Geophysical Prospecting*, 44(1), 131-152.

3 Loke, M. H. (2001), Constrained time-lapse resistivity imaging inversion, paper presented at  
4 Symposium on the Application of Geophysics to Engineering and Environmental Problems  
5 (SAGEEP), Denver, Colorado, March 4-7.

6 Loke, M. H., R. I. Acworth, and T. Dahlin (2003), A comparison of smooth and blocky  
7 inversion methods in 2D electrical imaging surveys, *Exploration Geophysics*, 34, 182-187.

8 Looms, M. C., K. H. Jensen, A. Binley, and L. Nielsen (2008), Monitoring unsaturated flow  
9 and transport using cross-borehole geophysical methods, *Vadose Zone Journal*, 7(1), 227-  
10 237.

11 Lucius, J.E., G.R. Olhoeft, P.L. Hill, and S.K. Duke (1992), Properties and hazards of 108  
12 selected substances - 1992 edition. Open-File Report 92-527, U. S. Geological Survey.

13 Newmark, R. L., W. D. Daily, K. R. Kyle, and A. L. Ramirez (1998), Monitoring DNAPL  
14 pumping using integrated geophysical techniques, *Journal of Environmental and Engineering*  
15 *Geophysics*, 3(1), 7-13.

16 Nimmer, R. E., J. L. Osiensky, A. M. Binley, and B. C. Williams (2008), Three-dimensional  
17 effects causing artifacts in two-dimensional, cross-borehole, electrical imaging, *Journal of*  
18 *Hydrology*, 359(1-2), 59-70.

19 Ogilvy, R. D., O. Kuras, P. I. Meldrum, P. B. Wilkinson, J. E. Chambers, M. Sen, A. Pulido-  
20 Bosch, J. Gisbert, S. Jorreto, I. Frances, and P. Tsourlos (2009), Automated Monitoring of  
21 Coastal Aquifers with Electrical Resistivity Tomography, *Near Surface Geophysics*, 7, 367-  
22 375.

1  
2  
3  
4  
5  
6  
7  
8  
9  
10  
11  
12  
13  
14  
15  
16  
17  
18  
19  
20  
21  
22  
23  
24  
25  
26  
27  
28  
29  
30  
31  
32  
33  
34  
35  
36  
37  
38  
39  
40  
41  
42  
43  
44  
45  
46  
47  
48  
49  
50  
51  
52  
53  
54  
55  
56  
57  
58  
59  
60  
61  
62  
63  
64  
65

---

1 Oldenborger, G. A., M. D. Knoll, P. S. Routh, and D. J. LaBrecque (2007), Time-lapse ERT  
2 monitoring of an injection/withdrawal experiment in a shallow unconfined aquifer,  
3 *Geophysics*, 72(4), F177-F187.

4 Pandit, N. S, and R.F. Miner (1986), Interpretation of slug test data. *Ground Water*, 24(6),  
5 743-749.

6 Pankow, J. F., and J. A. Cherry (1996), *Dense Chlorinated Solvents and other DNAPLs in*  
7 *Groundwater*, Waterloo Press, Portland, Oregon.

8 Pankow, J. F., S. Feenstra, J. A. Cherry, and M. C. Ryan (1996), Dense chlorinated solvents  
9 in groundwater: background and history of the problem, in *Dense chlorinated solvents and*  
10 *other DNAPLs in groundwater*, edited by J. F. Pankow and J. A. Cherry, pp. 1-52, Waterloo  
11 Press, Portland, Oregon.

12 Parasnis, D. S. (1988), Reciprocity theorems in geoelectric and geoelectromagnetic work,  
13 *Geoexploration*, 25(3), 177-198.

14 Parker, B. L., J. A. Cherry, S. W. Chapman, and M. A. Guilbeault (2003), Review and  
15 Analysis of Chlorinated Solvent Dense Nonaqueous Phase Liquid Distributions in Five  
16 Sandy Aquifers, *Vadose Zone Journal*, 2, 116-137.

17 Revil, A., L. M. Cathles, S. Losh, and J. A. Nunn (1998), Electrical conductivity in shaly  
18 sands with geophysical applications, *Journal of Geophysical Research-Solid Earth*,  
19 103(B10), 23925-23936.

20 Rivett, M. O., and L. Clark (2007), A quest to locate sites described in the world's first  
21 publication on trichloroethene contamination of groundwater, *Quarterly Journal of*  
22 *Engineering Geology and Hydrogeology*, 40, 241-249.

1  
2  
3  
4  
5  
6  
7  
8  
9  
10  
11  
12  
13  
14  
15  
16  
17  
18  
19  
20  
21  
22  
23  
24  
25  
26  
27  
28  
29  
30  
31  
32  
33  
34  
35  
36  
37  
38  
39  
40  
41  
42  
43  
44  
45  
46  
47  
48  
49  
50  
51  
52  
53  
54  
55  
56  
57  
58  
59  
60  
61  
62  
63  
64  
65

---

1 Roberts, J., S. Dworatzek, D. Major, E. Hood, M. Harkness, E. E. Mack, M. D. Lee, C. M.

2 Acheson, X. Mao, and B. Sleep (2008), TCE DNAPL bioremediation using partitioning  
3 electron donors, in *Sixth International Conference on Remediation of Chlorinated and*  
4 *Recalcitrant Compounds*, edited, pp. B-013, Monterey, California.

5 Sandberg, S. K., L. D. Slater and R. Versteeg (2002), An integrated geophysical investigation  
6 of the hydrogeology of an anisotropic unconfined aquifer, *Journal of Hydrology*, 267(3-4),  
7 227-243.

8 Sauck, W. A. (2000), A model for the resistivity structure of LNAPL plumes and their  
9 environs in sandy sediments, *Journal of Applied Geophysics*, 44(2-3), 151-165.

10 Schwille, F. (1988), *Dense chlorinated solvents in porous and fractured media*, 146 pp.,  
11 Lewis Publishers, Inc., Michigan, USA.

12 Shevnin, V., A. Mousatov, A. Ryjov, and O. Delgado-Rodriquez (2007), Estimation of clay  
13 content in soil based on resistivity modeling and laboratory measurements, *Geophysical*  
14 *Prospecting*, 55(2), 265-275.

15 Singha, K., and S. M. Gorelick (2005), Saline tracer visualized with three-dimensional  
16 electrical resistivity tomography: Field-scale spatial moment analysis, *Water Resources*  
17 *Research*, 41(5), W05023.

18 Singha, K., and S. M. Gorelick (2006), Hydrogeophysical tracking of three-dimensional  
19 tracer migration: The concept and application of apparent petrophysical relations, *Water*  
20 *Resources Research*, 42(6), W06422.

21 Slater, L. (2007), Near surface electrical characterization of hydraulic conductivity: from  
22 petrophysical properties to aquifer geometries – a review, *Surveys in Geophysics*, 28, 169-  
23 197.

- 
- 1 Slater, L., A. M. Binley, W. Daily and R. Johnson (2000), Cross-hole electrical imaging of a  
2 controlled saline tracer injection, *Journal of Applied Geophysics*, 44(2-3), 85-102.
- 3  
4  
5 3 Slater, L., A. Binley, R. Versteeg, G. Cassiani, R. Birken and S. Sandberg (2002), A 3D ERT  
6 study of solute transport in a large experimental tank, *Journal of Applied Geophysics*, 49(4),  
7  
8 4 211-229.  
9
- 10  
11  
12  
13 6 Tait, N. G., D. N. Lerner, J. W. N. Smith, and S. A. Leharne (2004), Prioritisation of  
14  
15 7 abstraction boreholes at risk from chlorinated solvent contamination on the UK Permo-  
16  
17 8 Triassic Sandstone aquifer using a GIS, *Science of the Total Environment*, 319(1-3), 77-98.  
19
- 20  
21 9 US EPA (Environmental Protection Agency) (2004), Site Characterisation Technologies for  
22  
23 10 DNAPL investigations, US Environmental Protection Agency, Washington, DC.  
24  
25  
26  
27 11 USEPA 2007, SW-846 Test Methods for Evaluating Solid Waste: Physical/Chemical  
28  
29 12 Methods: Revision 1, February 2007, US Environmental Protection Agency, Washington DC.  
30  
31  
32 13 Vogel, T. M. and P. L. McCarty (1985), Biotransformation of tetrachloroethylene to  
33  
34 14 trichloroethylene, dichloroethylene, vinyl chloride, and carbon dioxide under methanogenic  
35  
36 15 conditions. *Applied Environmental Microbiology*, 49, 1080–1083.  
37  
38  
39  
40 16 Weast, R. C. (1986), *CRC Handbook of Chemistry and Physics*, 67th ed., CRC Press, Boca  
41  
42 17 Raton, Florida.  
43  
44  
45 18 Weller, A., M. Grubne, M. Seichter and F. D. Borner (1996), Monitoring hydraulic  
46  
47 19 experiments by complex conductivity tomography, *European Journal of Environmental and*  
48  
49 20 *Engineering Geophysics*, 1, 209-228.  
50  
51  
52  
53 21 Wilkinson, P. B., J. E. Chambers, M. Lelliott, G. P. Wealthall, and R. D. Ogilvy (2008),  
54  
55 22 Extreme sensitivity of crosshole electrical resistivity tomography measurements to geometric  
56  
57 23 errors, *Geophysical Journal International*, 173(1), 49-62.  
58  
59  
60  
61
-

1  
2  
3  
4  
5  
6  
7  
8  
9  
10  
11  
12  
13  
14  
15  
16  
17  
18  
19  
20  
21  
22  
23  
24  
25  
26  
27  
28  
29  
30  
31  
32  
33  
34  
35  
36  
37  
38  
39  
40  
41  
42  
43  
44  
45  
46  
47  
48  
49  
50  
51  
52  
53  
54  
55  
56  
57  
58  
59  
60  
61  
62  
63  
64  
65

---

1 Wilkinson, P. B., P. I. Meldrum, O. Kuras, J. E. Chambers, S. J. Holyoake, and R. D. Ogilvy  
2 (2009), High-resolution Electrical Resistivity Tomography monitoring of a tracer test in a  
3 confined aquifer, *Journal of Applied Geophysics*, 70, 268-276.

4 Williams, K. H., A. Kemna, M. J. Wilkins, J. Druhan, E. Arntzen, A. L. N'Guessan, P. E.  
5 Long, S. S. Hubbard and J. F. Banfield (2009), Geophysical Monitoring of Coupled  
6 Microbial and Geochemical Processes During Stimulated Subsurface Bioremediation,  
7 *Environmental Science & Technology*, 43(17), 6717-6723.

8 Yi, M. J., J. H. Kim and S. H. Chung (2003), Enhancing the resolving power of least-squares  
9 inversion with active constraint balancing, *Geophysics*, 68(3), 931-941.

10 Zeeb, P., G. Wealthall, M. Lelliot, R. White, M. Rivett, S. Dwortzek, M. Harkness, M. Lee,  
11 D. Raymond, D. Ellis and L. Houlden (2008), Results from the SABRE field pilot test:  
12 Bioremediation of a TCE DNAPL source zone, in *Sixth International Conference on*  
13 *Remediation of Chlorinated and Recalcitrant Compounds*, edited, pp. B-005, Monterey,  
14 California.

15 Zhou, Q. Y., J. Shimada and A. Sato (2001), Three-dimensional spatial and temporal  
16 monitoring of soil water content using electrical resistivity tomography, *Water Resources*  
17 *Research*, 37(2), 273-285.

---

1 Figure 1. Research site plan showing the dimensions of the experimental cell, the location of  
2 the former MCA plant, and the positions of the source zone transect (SZT) and plume zone  
3 transect (PZT) ERT and multilevel sampler (MLS) arrays and the injection and monitoring  
4 wells. Inset shows location of study site within the UK.

5 Figure 2. Stratigraphic and lithological logs of the (a) SZT and (b) PZT.

6 Figure 3. Summary of groundwater chemistry changes in SZT and PZT during the  
7 experiment. Values are averages across each transect.

8 Figure 4. Cross-hole multi-channel measurement scheme used to collect ERT data on each  
9 panel. The dashed line joins the current electrodes, the dotted lines join sequential pairs of  
10 potential electrodes.

11 Figure 5. Mean absolute data sensitivity for the SZT. The white dashed lines indicate the  
12 intersection of the vertical and horizontal sections through the 3D sensitivity distribution.

13 Figure 6. Transect geology interpreted from (a) SZT boreholes, (b) SZT ERT model, (c) PZT  
14 boreholes and (d) PZT ERT model. See Figure 2 for SZT and PZT borehole logs.

15 Figure 7. Plots of in-hole dipole-dipole apparent resistivity data from the SZT borehole at  
16  $x = 2$  m. Raw data are shown by filled circles, interpolating lines were calculated by linear  
17 interpolation.

18 Figure 8. a) Horizontal section through a 3D resistivity model representing removed cores (10  
19  $\Omega\text{m}$ ) and disturbed zones (30  $\Omega\text{m}$ ) in a homogeneous background (100  $\Omega\text{m}$ ). b) 2.5D  
20 inversion of data from 3D model, exhibiting vertical banding associated with boreholes.

21 Figure 9. Time-lapse resistivity images of the SZT shown as a time series (top) and  
22 normalized images (bottom) for the baseline (b), Day 1 (d1), Day 150 (d150), Day 240

---

1 (d240), Day 420 (d420), Day 510 (d510) and Day 600 (d600) monitoring rounds. The  
2 bedrock is shown as a thick dashed line. The black masked areas at the top of the sections  
3 indicate the extent of the unsaturated zone. The dotted black box defines the approximate  
4 extent of the major preferential flow pathway towards the base of the gravels. The mean  
5 misfit errors are shown in the upper right corner of each resistivity image.

6 Figure 10. Time-lapse resistivity images of the PZT shown as a time series (top) and  
7 normalized images (bottom) for the baseline (b), Day 150 (d150), Day 240 (d240), Day 420  
8 (d420), Day 510 (d510) and Day 600 (d600) monitoring rounds. Bedrock shown as thick  
9 dashed line. The bedrock is shown as a thick dashed line. The black masked areas at the top  
10 of the sections indicate the extent of the unsaturated zone. The dotted black box defines the  
11 approximate extent of the major preferential flow pathway towards the base of the gravels.  
12 The mean misfit errors are shown in the upper right corner of each resistivity image.

13 Figure 11. Average change in resistivity towards base of gravels (in areas defined by dotted  
14 black boxes in Figure 9 and Figure 10) for the SZT and PZT.

15 Figure 12. Normalized resistivity image ( $\rho_b/\rho_{dl}$ ) showing the distribution of low resistivity  
16 electron donor (blue) two days after injection.

17 Figure 13. Kriged multi-level sampler (MLS) results from the SZT: (a) EC, (b) alkalinity, (c)  
18 chloride and (d) sulfate. The black dots show MLS sample locations. The black dashed line  
19 shows the inferred mudstone/gravel interface.

20 Figure 14. Kriged multi-level sampler (MLS) results from the PZT: (a) EC, (b) alkalinity, (c)  
21 chloride and (d) sulfate. The black dots show MLS sample locations. The black dashed line  
22 shows the inferred mudstone/gravel interface.

---

1 Figure 15. Average ERT derived resistivity, and MLS pore fluid EC, bicarbonate and  
2 chloride levels (in areas defined by dotted black boxes in Figure 9 and Figure 10) at the (a)  
3 SZT and the (b) PZT, and (c) variation in resistivity with bicarbonate concentration  
4 (Baseline to Day 600).

5 Figure 16. Plots of a) average bromide concentration, b) hydraulic conductivity and c)  
6 resistivity ratio ( $\rho_{d240}/\rho_b$ ) for the SZT, plus d) hydraulic conductivity and e) resistivity ratio  
7 for the PZT. The spatial correlation coefficients between the plots are shown in the inset  
8 table. The region b' comprises the area to the right of and below the white dashed line in b).  
9 MLS port and ERT electrode locations are shown as black dots. Areas with no data have been  
10 masked (white).

1  
2  
3  
4  
5  
6  
7  
8  
9  
10  
11  
12  
13  
14  
15  
16  
17  
18  
19  
20  
21  
22  
23  
24  
25  
26  
27  
28  
29  
30  
31  
32  
33  
34  
35  
36  
37  
38  
39  
40  
41  
42  
43  
44  
45  
46  
47  
48  
49  
50  
51  
52  
53  
54  
55  
56  
57  
58  
59  
60  
61  
62  
63  
64  
65

- 
- 1 Table 1. Mean groundwater temperatures recorded from MLS arrays during sampling.
  - 2 Table 2. Reciprocal error distributions and statistics for baseline data set.
  - 3 Table 3. Mean reciprocal errors for each monitoring round.
  - 4

**Table 1**[Click here to download Table: Table 1.pdf](#)1  
2  
3  
4  
5  
6  
7  
8  
9  
10  
11  
12  
13  
14  
15  
16  
17  
18  
19  
20  
21  
22  
23  
24  
25  
26  
27  
28  
29  
30  
31  
32  
33  
34  
35  
36  
37  
38  
39  
40  
41  
42  
43  
44  
45  
46  
47  
48  
49  
50  
51  
52  
53  
54  
55  
56  
57  
58  
59  
60  
61  
62  
63  
64  
65

<b>Monitoring Round</b>	<b>Mean Temperature (°C)</b>	<b>Standard Deviation (°C)</b>
<b>Baseline</b>	11.3	0.6
<b>d15</b>	14.9	0.6
<b>d240</b>	11.9	0.9
<b>d420</b>	13.1	0.7
<b>d510</b>	13.2	1.6
<b>d600</b>	11.0	1.5

**Table 2**[Click here to download Table: Table 2.pdf](#)

Reciprocal error	Fraction of data at or below reciprocal error level	
	SZT	PZT
<b>1%</b>	32.6%	24.3%
<b>2%</b>	55.4%	48.5%
<b>3%</b>	72.1%	65.3%
<b>4%</b>	82.5%	75.7%
<b>5%</b>	89.3%	83.4%
<b>10%</b>	99.3%	95.4%
<b>Reciprocal error statistics</b>		
<b>Mean</b>	2.31%	3.00%
<b>Standard deviation</b>	2.11%	2.96%
<b>Median</b>	1.72%	2.08%
<b>Inter-quartile range</b>	2.46%	2.86%

1  
2  
3  
4  
5  
6  
7  
8  
9  
10  
11  
12  
13  
14  
15  
16  
17  
18  
19  
20  
21  
22  
23  
24  
25  
26  
27  
28  
29  
30  
31  
32  
33  
34  
35  
36  
37  
38  
39  
40  
41  
42  
43  
44  
45  
46  
47  
48  
49  
50  
51  
52  
53  
54  
55  
56  
57  
58  
59  
60  
61  
62  
63  
64  
65

**Table 3**[Click here to download Table: Table 3.pdf](#)

<b>Monitoring round</b>	<b>Mean reciprocal error</b>	
	<b>SZT</b>	<b>PZT</b>
<b>Baseline</b>	2.31%	3.00%
<b>d1</b>	2.48%	-
<b>d150</b>	3.11%	1.60%
<b>d240</b>	2.90%	3.13%
<b>d420</b>	2.51%	3.33%
<b>d510</b>	2.92%	2.01%
<b>d600</b>	2.18%	2.32%

1  
2  
3  
4  
5  
6  
7  
8  
9  
10  
11  
12  
13  
14  
15  
16  
17  
18  
19  
20  
21  
22  
23  
24  
25  
26  
27  
28  
29  
30  
31  
32  
33  
34  
35  
36  
37  
38  
39  
40  
41  
42  
43  
44  
45  
46  
47  
48  
49  
50  
51  
52  
53  
54  
55  
56  
57  
58  
59  
60  
61  
62  
63  
64  
65

Figure 1

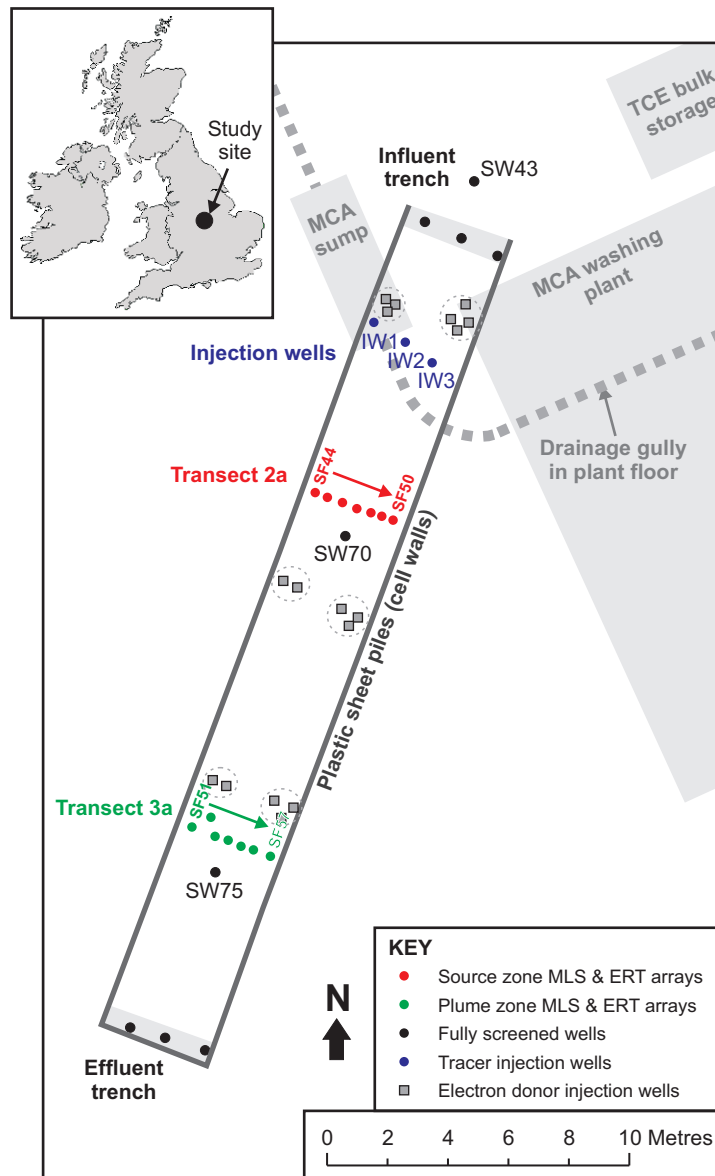


Figure 2

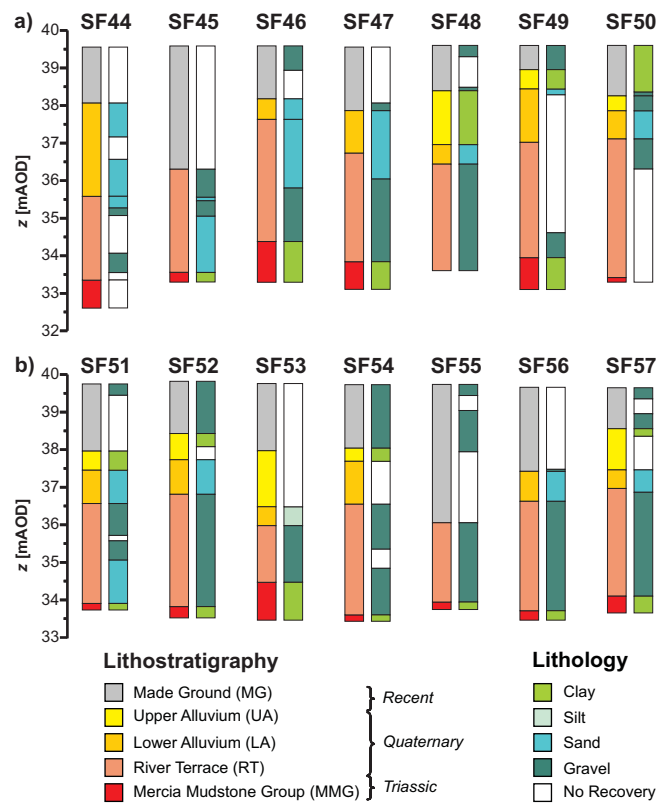


Figure 3

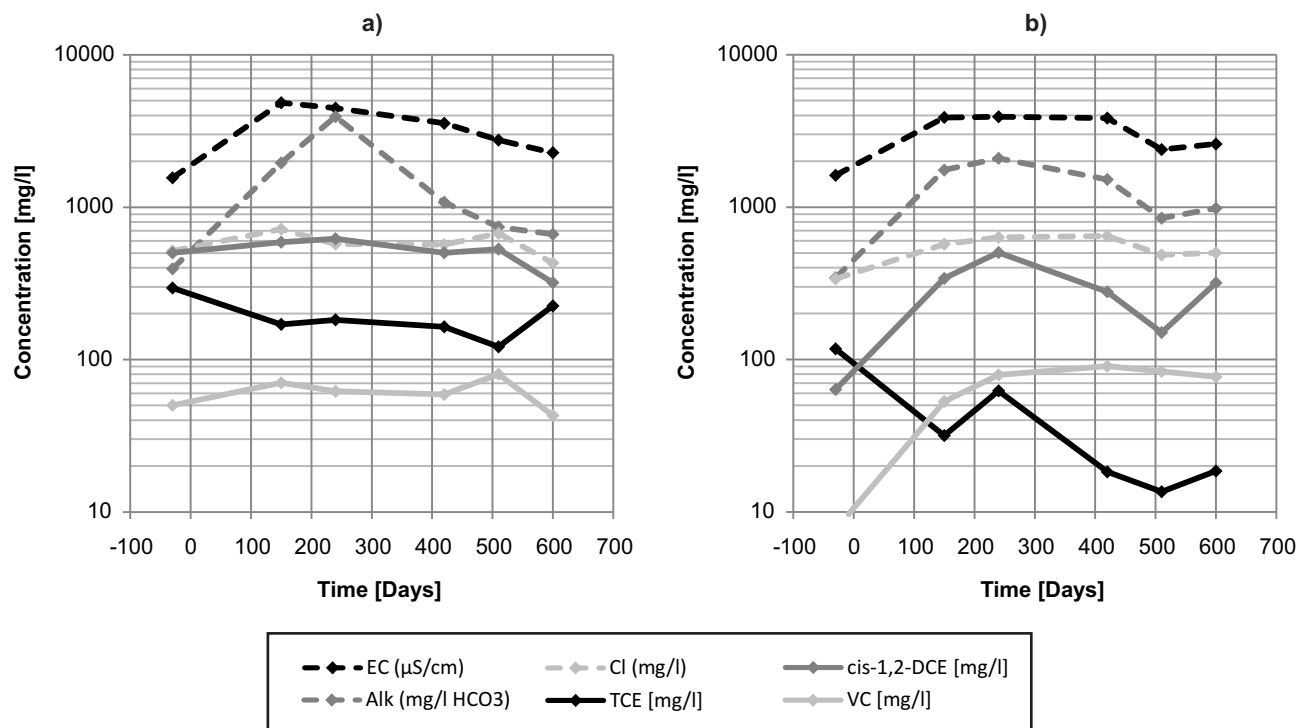


Figure 4

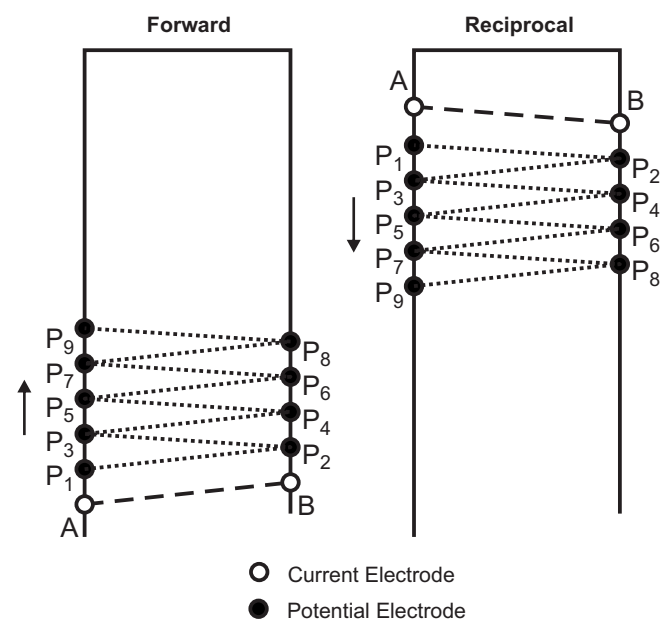


Figure 5

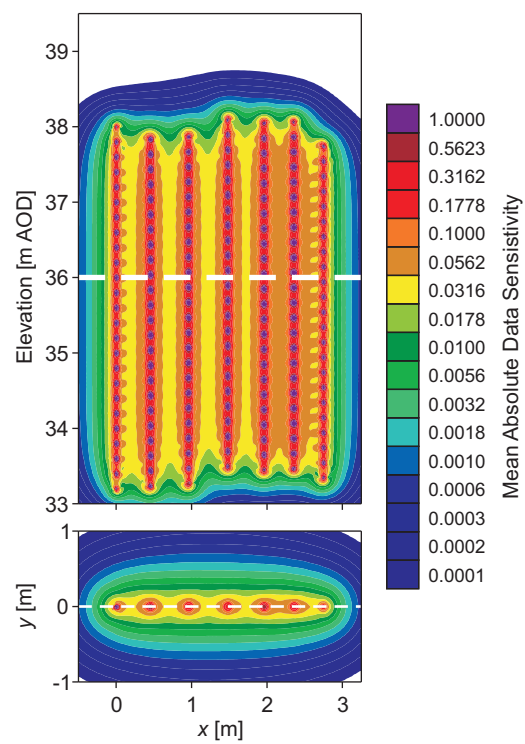


Figure 6

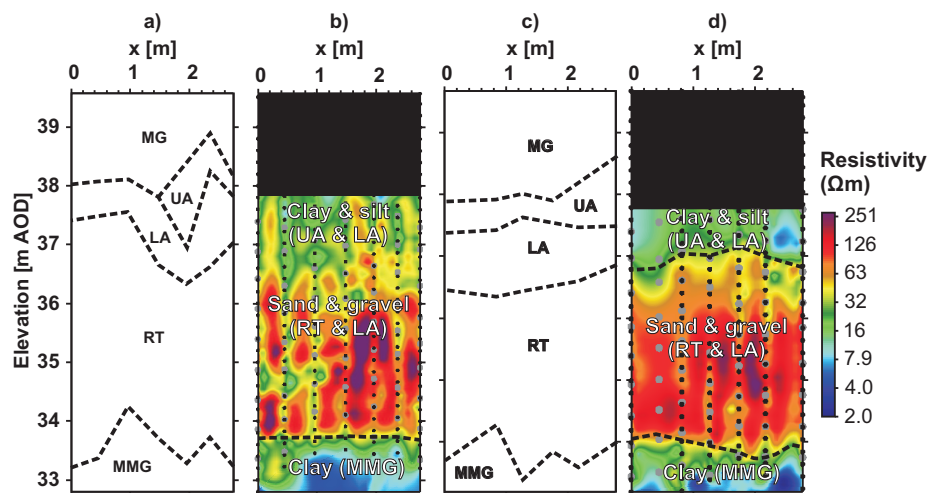


Figure 7

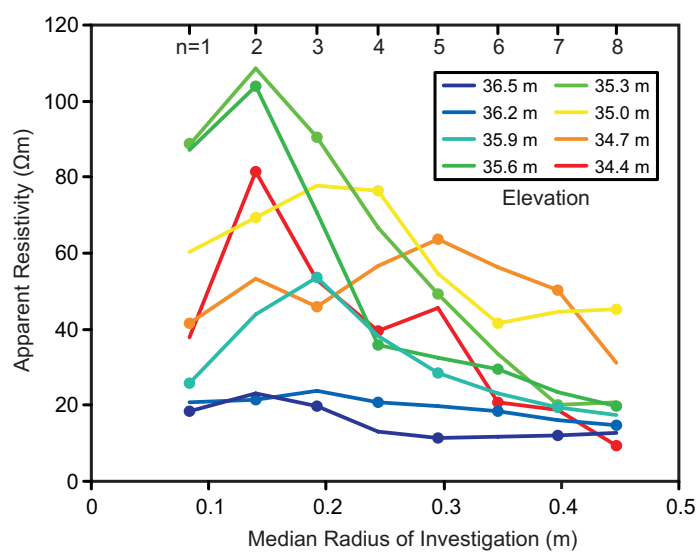


Figure 8

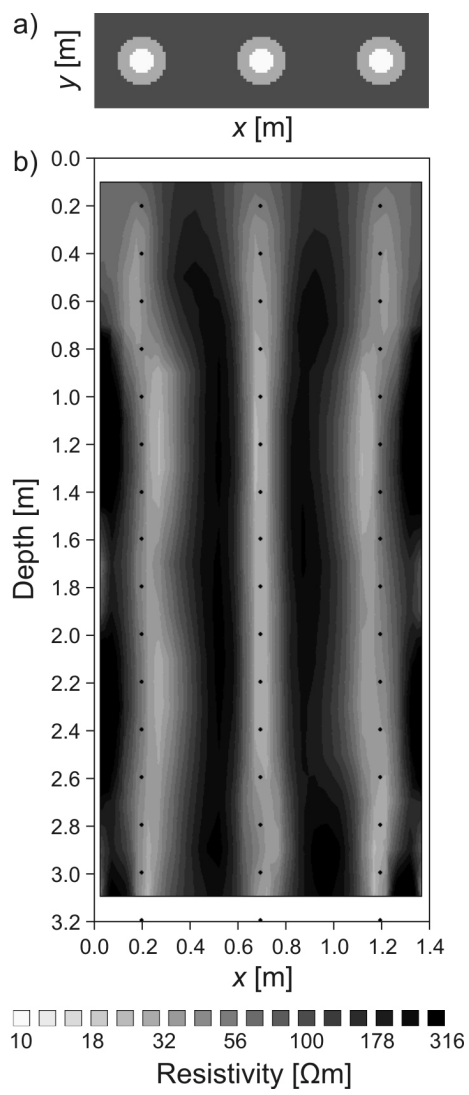


Figure 9

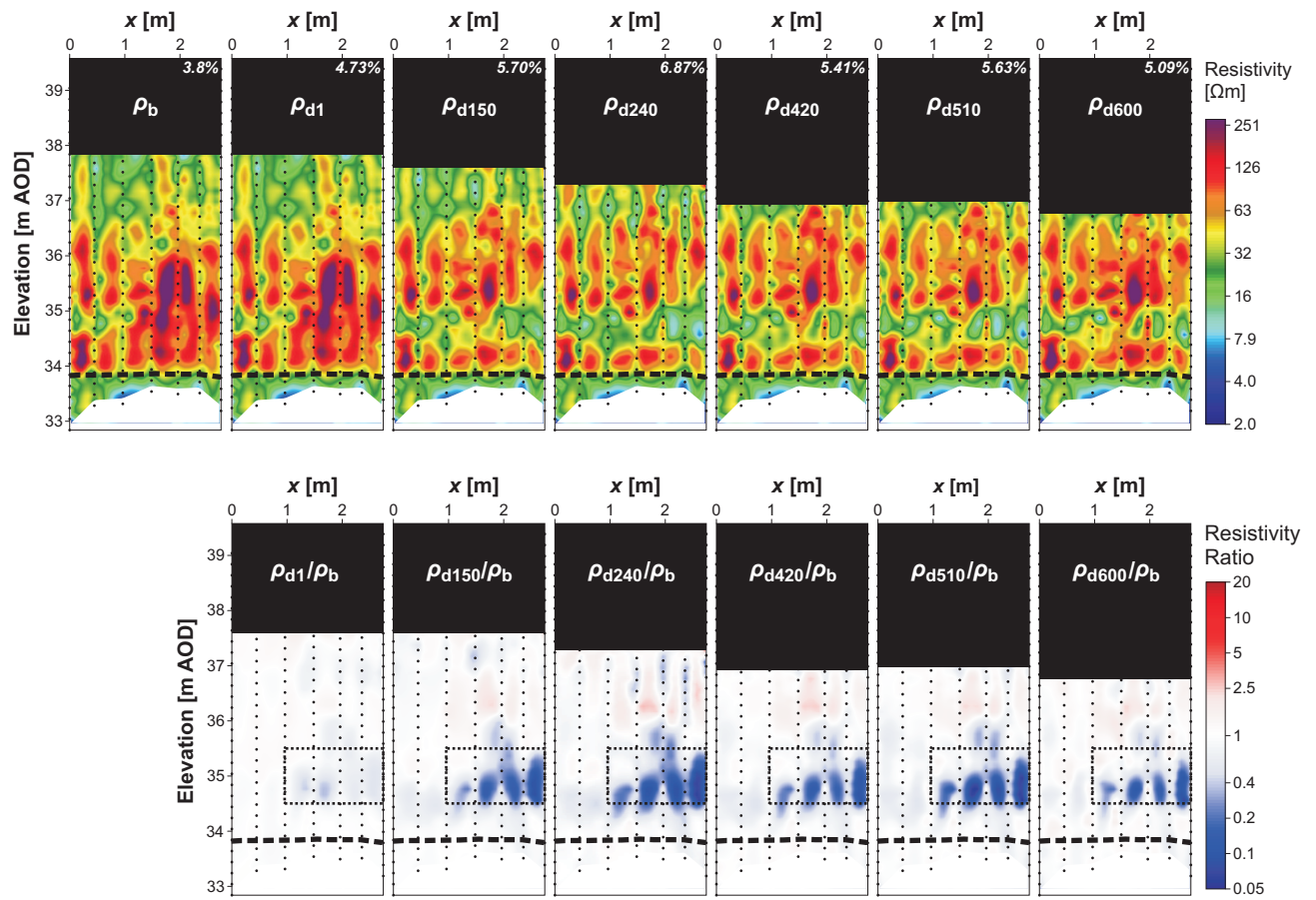


Figure 10

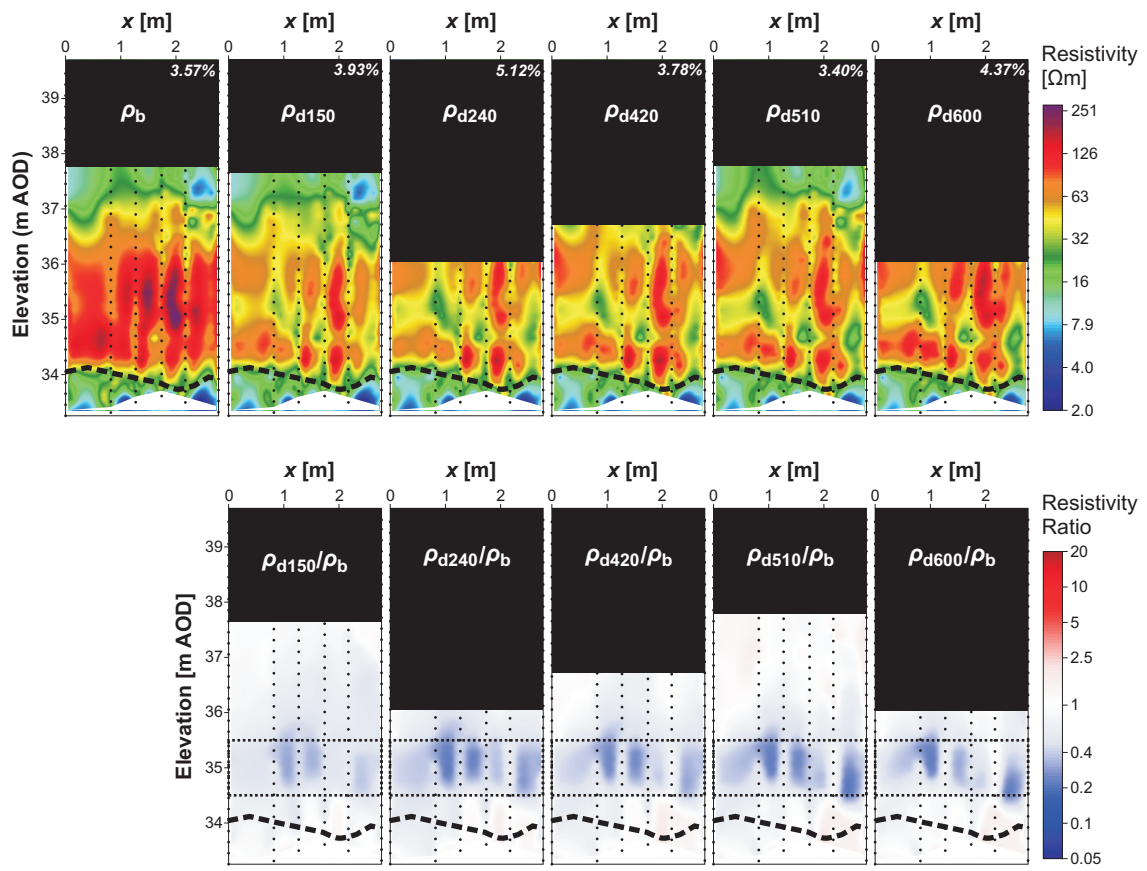


Figure 11

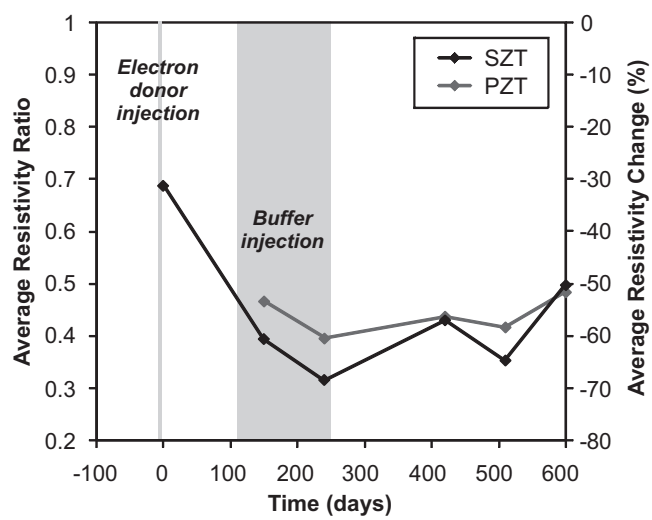


Figure 12

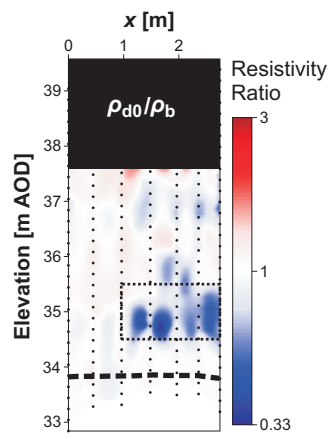


Figure 13

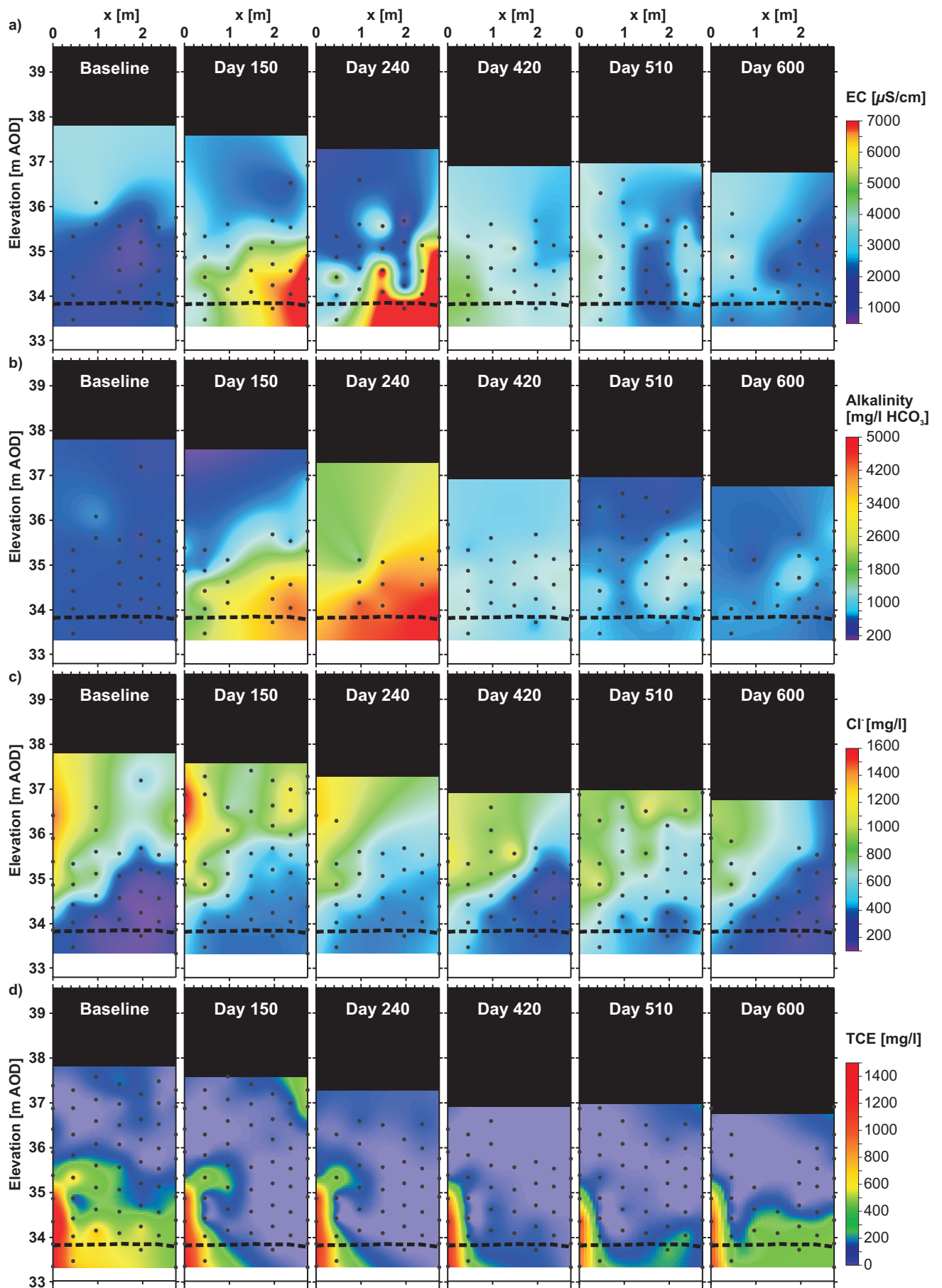


Figure 14

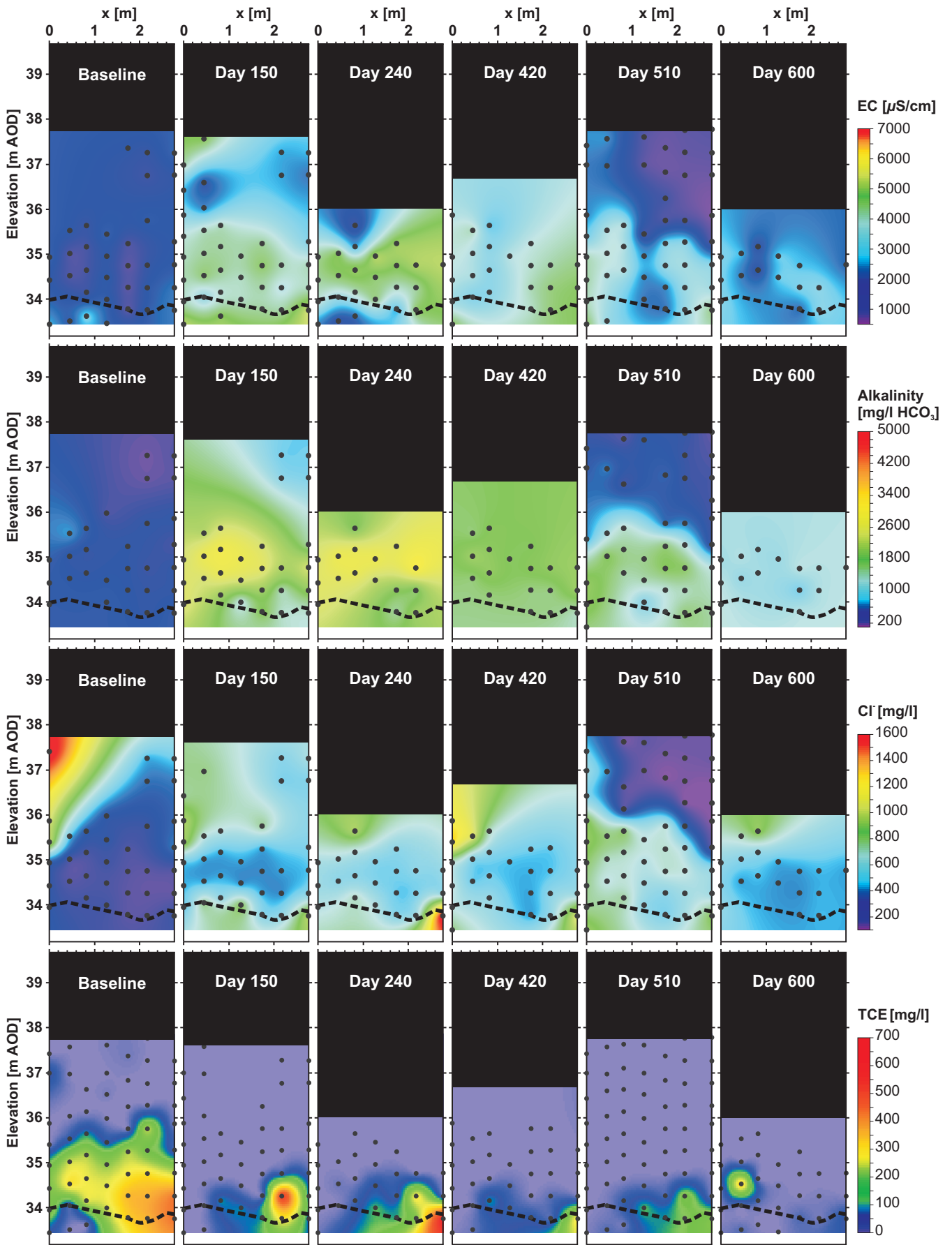


Figure 15

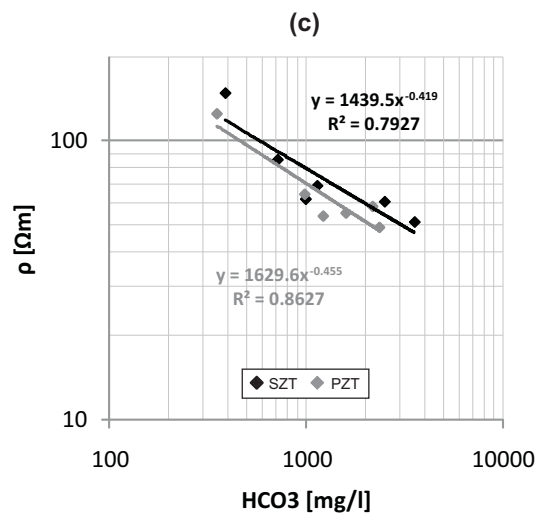
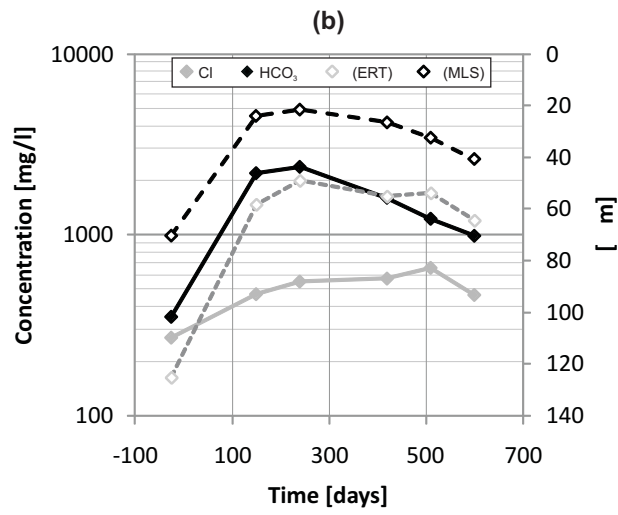
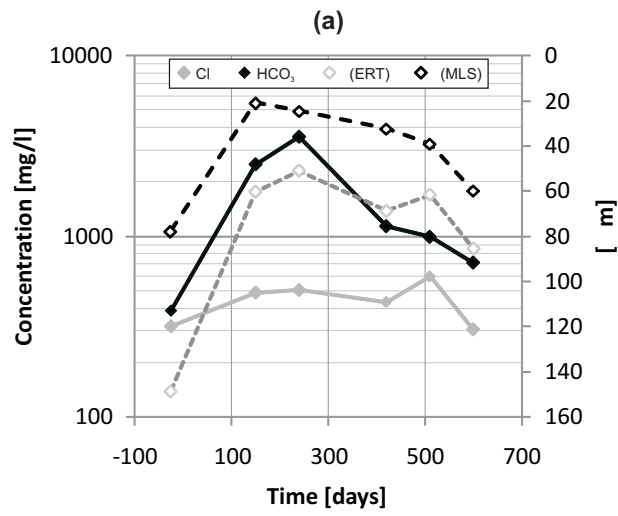


Figure 16

